iScience

CellPress
OPEN ACCESS

Article

BAD-mediated neuronal apoptosis and neuroinflammation contribute to Alzheimer's disease pathology

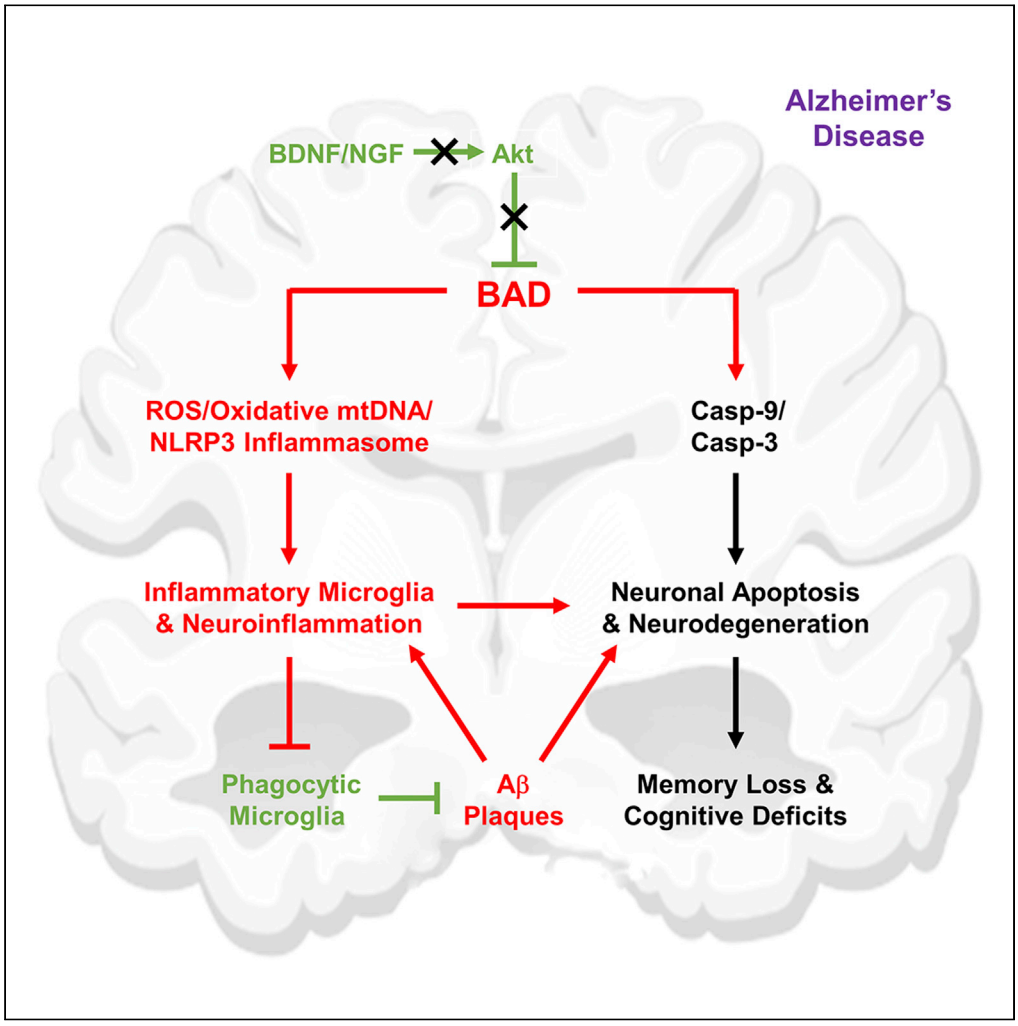

Liansheng Zhang, Yun Qian, Jie Li, ..., Xiaohua Cao, Naihe Jing, Anning Lin

njing@sibcb.ac.cn (N.J.)
anninglin@nju.edu.cn (A.L.)

Highlights

BAD contributes to neuronal apoptosis in murine models and in patients with AD

Reduced Akt activation is responsible for enhanced neuronal BAD apoptotic activity

Bad loss inhibits Aβ deposition by promoting microglial phagocytosis

BAD promotes microglial NLRP3 inflammasome activation via ROS-mtDNA axis

Zhang et al., iScience *24*, 102942
September 24, 2021
https://doi.org/10.1016/j.isci.2021.102942

iScience

CellPress
OPEN ACCESS

Article

BAD-mediated neuronal apoptosis and neuroinflammation contribute to Alzheimer's disease pathology

Liansheng Zhang,[1,2,3] Yun Qian,[1] Jie Li,[1,3,4] Xuan Zhou,[5] He Xu,[1,4] Jie Yan,[6] Jialing Xiang,[7] Xiang Yuan,[1,2,3] Beicheng Sun,[8] Sangram S. Sisodia,[9,10] Yong-Hui Jiang,[11] Xiaohua Cao,[5] Naihe Jing,[1,4,12,13,*] and Anning Lin[2,3,9,14,15,*]

SUMMARY

Alzheimer's disease (AD) is the most common progressive neurodegenerative disease. However, the underlying molecular mechanism is incompletely understood. Here we report that the pro-apoptotic protein BAD as a key regulator for neuronal apoptosis, neuroinflammation and Aβ clearance in AD. BAD pro-apoptotic activity is significantly increased in neurons of AD patients and 5XFAD mice. Conversely, genetic disruption of *Bad* alleles restores spatial learning and memory deficits in 5XFAD mice. Mechanistically, phosphorylation and inactivation of BAD by neurotropic factor-activated Akt is abrogated in neurons under AD condition. Through reactive oxygen species (ROS)-oxidized mitochondrial DNA (mtDNA) axis, BAD also promotes microglial NLRP3 inflammasome activation, thereby skewing microglia toward neuroinflammatory microglia to inhibit microglial phagocytosis of Aβ in AD mice. Our results support a model in which BAD contributes to AD pathologies by driving neuronal apoptosis and neuroinflammation but suppressing microglial phagocytosis of Aβ, suggesting that BAD is a potential therapeutic target for AD.

INTRODUCTION

Alzheimer's disease (AD), the most common form of dementia, is a progressive neurodegenerative disease that is characterized by deposition of Aβ plaques, accumulation of neurofibrillary tangles, neuronal loss, and neuroinflammation (Association, 2019; Long and Holtzman, 2019; Querfurth and LaFerla, 2010). Overwhelming evidence shows that accumulation of Aβ plaques induces progressive neuronal degeneration and synaptic loss, resulting in severe neuronal loss and subsequent memory and cognitive deficits in AD patients and animal models (Crews and Masliah, 2010). Emerging evidence also shows that Aβ promote activation of inflammatory microglia, the brain resident macrophages, which suppress and prevent phagocytic microglia from clearing Aβ plaques, thereby aggravating the pathology of AD (Heneka et al., 2013; Tejera et al., 2019). A better understanding of the molecular mechanism that drives the pathogenesis is crucial for developing effective therapeutic strategies for AD.

Neuronal loss in AD has been reported to possess certain features of apoptosis, pyroptosis (programmed necrosis) or necroptosis (Caccamo et al., 2017; Cotman and Su, 1996; Tan et al., 2014). DNA fragmentation and caspase-3 activation are found in neurons in patients with AD (Cotman and Su, 1996; Su et al., 2002), while Aβ is capable of inducing neuronal apoptosis *in vitro* (Biswas et al., 2007; Kudo et al., 2012), suggesting that apoptosis is involved in neuronal loss in AD. In addition, expression of several pro- and anti-apoptotic members of the BCL-2 family, such as BCL-2, BCL-XL, BAX, BAK, BAD and BIM, are changed in brain extracts of AD patients (Avelina et al., 1998; Kitamura et al., 1998) or involved in Aβ-induced neuronal apoptosis in cell culture experiments (Biswas et al., 2007; Feng et al., 2015; Kudo et al., 2012). Overexpression of BCL-2 in 3xTg AD mice also improves place recognition memory (Rohn et al., 2008). On the other hand, NLRP1, a key component in pyroptosis, is upregulated in neurons in the AD mouse model, while knockdown of NLRP1 or caspase-1, another key component in pyroptosis, reduces neuronal death and reverses cognitive impairments (Tan et al., 2014), indicating that pyroptosis contributes to neuronal loss in AD. In addition, expression levels of RIPK1 and MLKL, two key components of necroptosis,

[1]The State Key Laboratory of Cell Biology, CAS Center for Excellence in Molecular Cell Science, Institute of Biochemistry and Cell Biology, Chinese Academy of Sciences; University of Chinese Academy of Sciences, Shanghai 200031, China

[2]Institute of Modern Biology, Nanjing University, Nanjing 210023, China

[3]Ben May Department for Cancer Research, The University of Chicago, Chicago, IL 60637, USA

[4]School of Life Science and Technology, ShanghaiTech University, Shanghai 201210, China

[5]Key Laboratory of Brain Functional Genomics, Ministry of Education, School of Life Sciences, East China Normal University, Shanghai 200062, China

[6]The Second Affiliated Hospital, The State Key Laboratory of Respiratory Disease, Guangdong Provincial Key Laboratory of Allery & Clinical Immunology, Guangzhou Medical University, Guangzhou, Guangdong 510260, China

[7]Department of Biological and Chemical Sciences, Illinois Institute of Technology, Chicago, IL 60616, USA

[8]Department of Hepatobiliary Surgery, The Affiliated Drum Tower Hospital of Nanjing University Medical School, Nanjing 210008, Jiangsu Province, China

[9]Department of Neurobiology, The University of Chicago, Chicago, IL 60637, USA

[10]The Microbiome Center, The University of Chicago, Chicago, IL 60637, USA

Continued

are increased in brain tissues of patients with AD, while overexpression of MLKL in neurons exacerbates cognitive deficits and necroptosis inhibitor Nec-1 is able to prevent neurodegeneration in AD mouse models (Caccamo et al., 2017), indicating necroptosis may also be involved in neuronal loss in AD. Although apoptosis, pyroptosis, or necroptosis may all contribute to AD, the pathological relevance and genetic evidence of a specific component(s) of the programmed cell death machinery that is responsible for neuropathology and memory deficits in AD remain elusive, so is the underlying mechanism.

Recent studies reveal that neuroinflammation has a crucial function in the development of AD (Heneka et al., 2013; Ising et al., 2019; Tejera et al., 2019). Neuroinflammation is mediated by neuroinflammatory microglia and neurotoxic A1 astrocytes (Liddelow et al., 2017), which are typically co-localized with fibrillary plaques and have elevated levels of biochemical markers and proinflammatory cytokines in the patient brains (Querfurth and LaFerla, 2010). Aβ is a key stimulus of neuroinflammatory microglia through activation of microglial NLRP3 inflammasome (Halle et al., 2008). Aβ can be sensed by microglial pattern recognition receptors, such as Toll-like receptor 2 (TLR-2) (Liu et al., 2012) and CD36 (Yamanaka et al., 2012), thereby engulfed by microglia through phagocytosis and degraded by lysosomes (Tarasoff-Conway et al., 2015). However, chronic exposure to Aβ results in activation of microglia, as engulfed Aβ induce lysosomal damage to induce NF-κB-dependent transcription of NLRP3 and pro-IL-1β (Heneka et al., 2015b) and subsequent assembly and activation of NLRP3 inflammasome to activate caspase-1 (Halle et al., 2008), which in turn triggers pro-IL-1β processing and mature IL-1β release (Martinon et al., 2002) for neuroinflammation. On the other hand, activation of NLRP3 inflammasome compromises phagocytic microglia-mediated clearance of Aβ plaques, thereby providing a crosstalk between neuroinflammatory and phagocytic microglia in AD (Tejera et al., 2019). Furthermore, neuroinflammatory microglia can induce the activation of neurotoxic A1 astrocytes by secreting TNFα, IL-1α, and C1q, which induce neuronal apoptosis via releasing an unknown toxic factor (Liddelow et al., 2017), thereby contributing to neuronal death in AD. However, the regulatory mechanism underlying NLRP3 inflammasome activation in AD is poorly understood.

The pro-apoptotic BCL-2 family member BAD plays a critical role in regulating mitochondrial-dependent and caspase-mediated apoptosis (Danial, 2008). BAD is typically phosphorylated and thereby inactivated by growth/survival factor-activated protein kinases, e.g., phosphorylation at Ser136 by growth factor-activated Akt (Datta et al., 1997), or by pro-inflammatory cytokine TNFα-activated IKK at Ser26 (Yan et al., 2013). Hypo-phosphorylated BAD will translocate to the mitochondrial outer membrane, where it inactivates the anti-apoptotic BCL-2 family proteins BCL-2 and BCL-XL to trigger the mitochondria-dependent apoptosis (Yang et al., 1995). Although BAD protein level is increased in membranous fractions of the temporal cortex of AD patients (Kitamura et al., 1998) or in platelets of AD patients (Zhao et al., 2016), there is no genetic link or causative relationship between BAD with the deficits in spatial learning and memory of AD in genetic animal models or patients specimens. Here, we show that BAD contributes to memory deficits and neuropathology in AD by promoting neuronal apoptosis and neuroinflammation, while inhibiting microglial phagocytosis of Aβ, thereby identifying BAD as a potential therapeutic target for AD.

RESULTS

BAD is involved in the pathogenesis of Alzheimer's disease

To determine whether BAD involves in neuronal death in AD, we examined BAD pro-apoptotic activity and neuronal apoptosis in the brain tissues of patients with AD and age-matched controls (see Table S1 for case information). Cell fractionation assay showed that BAD translocation from cytosol to mitochondria was significantly increased (~2 fold) in hippocampal and frontal cortical tissues of patients with AD compared with age-matched controls (Figures 1A and 1B). This is not the result that brain BAD expression is changed in AD, as BAD protein levels in the brain tissues were similar between patients and normal controls (Figures 1A and 1B). More importantly, immunofluorescent staining revealed that mitochondrial translocation of BAD was significantly increased in frontal cortical neurons of patients with AD compared with the controls, along with enhanced activation of caspase-3 (Casp-3), which is a specific executioner caspase in apoptosis (Figures 1C and 1D), indicating that BAD contributes to neuronal apoptosis in patients with AD.

To interrogate the role of BAD in the pathology of AD and the underlying mechanism, we used 5XFAD mice, which is a murine model of AD featured with severe neuronal loss, neuroinflammation, and behavioral alterations when aged (Oakley et al., 2006). *Bad*$^{-/-}$ mice were crossed into 5XFAD mice to generate 5XFAD/*Bad*$^{-/-}$ mice (Figure S1A). Morris water maze test was used to assess spatial learning and memory of 6-month-old wild type (WT) littermate, 5XFAD and 5XFAD/*Bad*$^{-/-}$ mice. As expected, 5XFAD mice

[11]Department of Pediatrics and Neurobiology, Duke University School of Medicine, Durham, NC 27710, USA

[12]CAS Key Laboratory of Regenerative Biology, Guangdong Provincial Key Laboratory of Stem Cell and Regenerative Medicine, Guangzhou Institutes of Biomedicine and Health, Chinese Academy of Sciences, Guangzhou 510530, China

[13]Center of Cell Lineage and Atlas, Guangzhou Regenerative Medicine and Health Guangdong Laboratory (GRMH-GDL), Guangzhou 510005, China

[14]Grossman Institute for Neuroscience, Quantitative Biology, and Haman Behavior, The University of Chicago, Chicago, IL 60637, USA

[15]Lead contact

*Correspondence: njing@sibcb.ac.cn (N.J.), anninglin@nju.edu.cn (A.L.)

https://doi.org/10.1016/j.isci.2021.102942

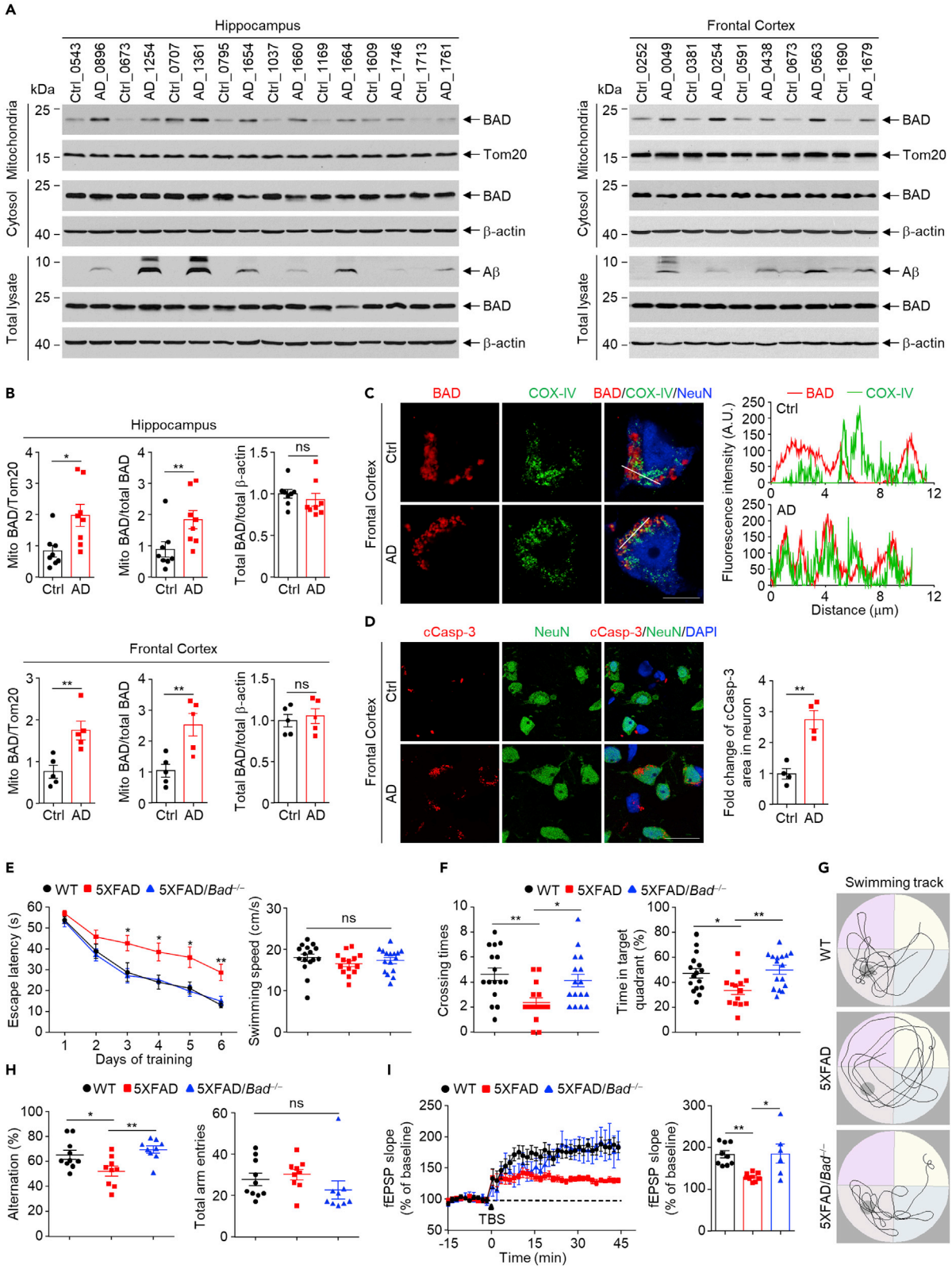
A
Hippocampus
Frontal Cortex
kDa
Ctrl_0543
AD_0896
Ctrl_0673
AD_1254
Ctrl_0707
AD_1361
Ctrl_0795
AD_1654
Ctrl_1037
AD_1660
Ctrl_1169
AD_1664
Ctrl_1609
AD_1746
Ctrl_1713
AD_1761
Ctrl_0252
AD_0049
Ctrl_0381
AD_0254
Ctrl_0591
AD_0438
Ctrl_0673
AD_0563
Ctrl_1690
AD_1679
Mitochondria
Cytosol
Total lysate
BAD
Tom20
β-actin
Aβ
B
Hippocampus
Frontal Cortex
Mito BAD/Tom20
Mito BAD/total BAD
Total BAD/total β-actin
Ctrl
AD
ns
C
BAD
COX-IV
BAD/COX-IV/NeuN
Fluorescence intensity (A.U.)
Distance (μm)
D
cCasp-3
NeuN
cCasp-3/NeuN/DAPI
Fold change of cCasp-3 area in neuron
E
WT
5XFAD
5XFAD/Bad-/-
Escape latency (s)
Days of training
Swimming speed (cm/s)
F
Crossing times
Time in target quadrant (%)
G
Swimming track
H
Alternation (%)
Total arm entries
I
fEPSP slope (% of baseline)
TBS
Time (min)

Figure 1. BAD pro-apoptotic activity is increased in hippocampal and frontal cortical neurons of patients with Alzheimer's disease and contributes to spatial learning and memory deficits in 5XFAD mice

(A) Detection of BAD mitochondrial translocation in hippocampus and frontal cortex of patients with Alzheimer's disease and age-matched healthy control brains.

(B) Quantification of the ratio of mitochondrial BAD to Tom20, the ratio of mitochondrial BAD to total BAD and the ratio of total BAD to total β-actin in hippocampus (n = 8) and frontal cortex (n = 5). Data were presented as mean ± SEM. *p < 0.05, **p < 0.01, student's *t*-test.

(C) Confocal image of co-localization of BAD with mitochondria in frontal cortical neurons of patients with Alzheimer's disease and age-matched healthy control brains (left panels). Scale bar, 10 μm. The co-localization of BAD and mitochondria was analyzed by the overlap of BAD and COX-IV immunofluorescent signals (right panels).

(D) Double immunofluorescent staining of active cleaved Casp-3 (cCasp-3) and NeuN in frontal cortical neurons of patients with Alzheimer's disease and age-matched healthy control brains. Scale bar, 20 μm. The average area of cCasp-3 in frontal cortical neurons was quantified (n = 4). Data were presented as mean ± SEM. **p < 0.01, student's *t*-test.

(E) Escape latency of 6-month-old WT (n = 16), 5XFAD (n = 14) and 5XFAD/*Bad*$^{-/-}$ (n = 16) mice in Morris water maze test. Data were presented as mean ± SEM. *p < 0.05, **p < 0.01, one-way ANOVA followed by Tukey's *post hoc* test. The swimming speed of the first trial on day 1 in Morris water maze test was analyzed. Data were presented as mean ± SEM. One-way ANOVA test.

(F) Target crossing times and the time (%) spent in target quadrant in the probe test of Morris water maze test. Data were presented as mean ± SEM. *p < 0.05, **p < 0.01, one-way ANOVA test.

(G) Representative swimming track plots of WT, 5XFAD and 5XFAD/*Bad*$^{-/-}$ mice in the probe test of Morris water maze test.

(H) Spatial memory of 6-month-old WT (n = 10), 5XFAD (n = 9), 5XFAD/*Bad*$^{-/-}$ (n = 9) mice were tested by spontaneous alternation Y-maze test. Data were presented as mean ± SEM. *p < 0.05, **p < 0.01, one-way ANOVA test.

(I) Long-term potentiation (LTP) induced by theta burst stimulation (TBS) was recorded at hippocampus CA3-CA1 pathway for 8-month-old WT (n = 9), 5XFAD (n = 9) and 5XFAD/*Bad*$^{-/-}$ (n = 6) mice, and the field excitatory postsynaptic potentials (fEPSP) of the last 10 min recording were quantified. Data were presented as mean ± SEM. *p < 0.05, **p < 0.01, one-way ANOVA test.

See also Figure S1 and Table S1.

displayed severe loss of spatial learning and memory compared with WT mice. By contrast, 5XFAD/*Bad*$^{-/-}$ mice were almost completely protected from spatial learning and memory deficits (Figures 1E–1G). Consistently, while 5XFAD mice showed significantly poor performance compared with WT mice in the spontaneous alternation Y-maze test, 5XFAD/*Bad*$^{-/-}$ mice performed as well as WT mice (Figure 1H). *Bad* loss did not affect spatial learning and memory in WT mice (Figure S1B), suggesting that BAD is only involved in impairing spatial learning and memory in mice with AD. This notion was further supported by the analysis of long-term potentiation (LTP), which measures the hippocampal synaptic plasticity that represents the newly formed declarative memories (Nicoll, 2017). The LTP was suppressed in hippocampal slices prepared from 5XFAD mice compared with WT control and the suppression was restored in 5XFAD/*Bad*$^{-/-}$ mice (Figure 1I), suggesting that BAD contributes to the cognitive dysfunction. Taken together, *Bad* loss restores behavioral alterations and cognitive malfunctions in the 5XFAD mouse model.

BAD-mediated neuronal apoptosis contributes to neurodegeneration and neuronal loss in 5XFAD mice

Given significantly increased pro-apoptotic activity of BAD along with enhanced Casp-3 activation in frontal cortical neurons in patients with AD (Figures 1A–1D) and *Bad* loss restored spatial learning and memory deficits in 5XFAD mice (Figures 1E–1H), we hypothesized that BAD has a crucial role in mediating neurodegeneration and neuronal loss in 5XFAD mice. We found that the cortical layer 5, subiculum, and dentate gyrus of 9-month-old 5XFAD mice had significantly reduced neuron density compared with WT mice, as expected (Oakley et al., 2006). By contrast, reduction of neuronal density in cortical layer 5 and dentate gyrus was prevented and neuronal loss in subiculum of hippocampus was partially rescued in 5XFAD/*Bad*$^{-/-}$ mice when compared with WT mice (Figures 2A and 2B). Similar results were obtained when degenerated neurons were analyzed by Fluoro-Jade C (FJC), a specific neurodegeneration marker, in brain slices of 6- and 9-month-old WT, 5XFAD and 5XFAD/*Bad*$^{-/-}$ mice (Figures 2C and 2D). This is not the result that BAD affects basal neuronal density, as *Bad* loss alone did not affect neuronal density in 9-month-old WT mice (Figures S1C and S1D). Interestingly, there was no significantly dynamic difference in the density of degenerated neurons between 6- and 9-month-old 5XFAD and 5XFAD/*Bad*$^{-/-}$ mice, most likely because the number of degenerated neurons in cortical layer 5 or hippocampus was very low and neurodegeneration was a slowly progressive process (Figures 2C and 2D). These results demonstrate a progressive but significant BAD-dependent neurodegeneration and neuronal loss in 5XFAD mice.

We next determined whether BAD promotes neurodegeneration and neuronal loss by triggering neuronal apoptosis in 5XFAD mice. Cell fractionation assay revealed that mitochondrial BAD was significantly increased in brain tissues of 9-month-old 5XFAD mice compared with that in WT mice (Figure 2E), while BAD protein level

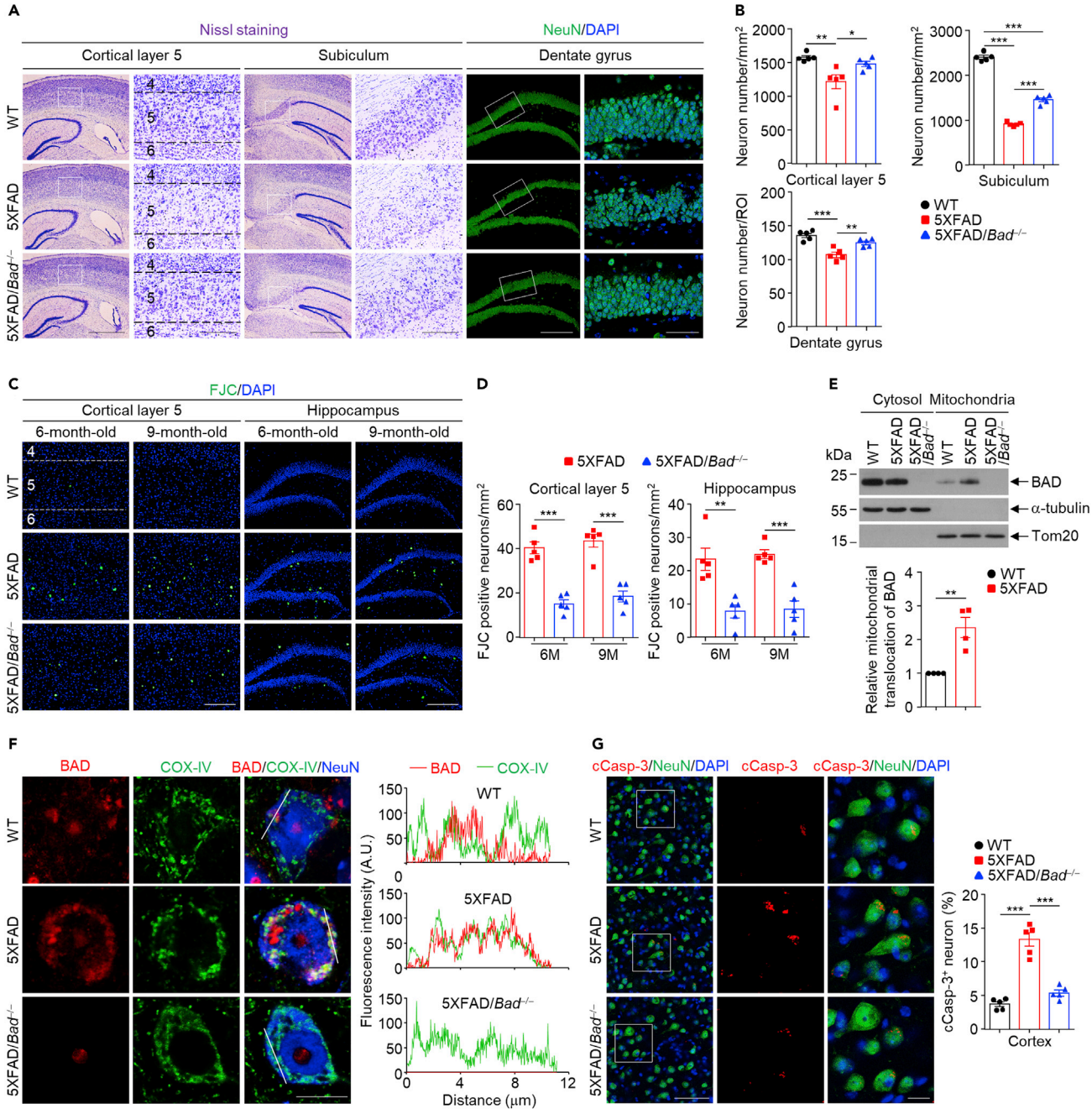

Figure 2. *Bad* loss suppresses neuronal degeneration and neuronal loss in 5XFAD mice

(A) Neuronal loss was analyzed in 9-month-old WT, 5XFAD and 5XFAD/*Bad*$^{-/-}$ mice. Neuronal density in cortical layer 5 of cortex and subiculum of hippocampus was analyzed by Nissl staining. Scale bar, 1.0 mm; magnified inset, 200 μm. Neuronal density in dentate gyrus of hippocampus was analyzed by immunofluorescent staining with anti-NeuN antibody. Scale bar, 200 μm; magnified inset, 50 μm.

(B) Quantification of neuronal density in cortical layer 5, subiculum and dentate gyrus (n = 5). Data were presented as mean ± SEM. *p < 0.05, **p < 0.01, ***p < 0.001, one-way ANOVA test.

(C) Degenerated neurons in cortical layer 5 and hippocampus of 6- and 9-month-old WT, 5XFAD and 5XFAD/*Bad*$^{-/-}$ mice were detected by Fluoro-Jade C (FJC) staining. Scale bar, 200 μm.

(D) Quantification of FJC positive neurons in cortical layer 5 and hippocampus of 6- and 9-month-old 5XFAD and 5XFAD/*Bad*$^{-/-}$ mice (n = 5). Data were presented as mean ± SEM. **p < 0.01, ***p < 0.001, student's *t*-test.

Figure 2. *Continued*

(E) Detection of BAD mitochondrial translocation by cytosol/mitochondria fractionation in brains of 9-month-old WT and 5XFAD mice. Age-matched 5XFAD/*Bad*$^{-/-}$ mice were used as control. The band intensity of BAD in mitochondrial part was normalized to Tom20 (n = 4). Data were presented as mean ± SEM. **p < 0.01, student's *t*-test.

(F) Confocal image of the staining of BAD, COX-IV and NeuN in cortical neurons of 9-month-old WT, 5XFAD and 5XFAD/*Bad*$^{-/-}$ mice (left panels). Scale bar, 10 μm. The co-localization of BAD with mitochondria was analyzed by the overlap of BAD and COX-IV immunofluorescent signals (right panels).

(G) Double staining of cCasp-3 and NeuN in cortex neurons of 9-month-old WT, 5XFAD and 5XFAD/*Bad*$^{-/-}$ mice. Scale bar, 50 μm; magnified inset, 10 μm. The percentage of cCasp-3 positive neurons in cortex was quantified (n = 5). Data were presented as mean ± SEM. ***p < 0.001, one-way ANOVA test. See also Figures S2–S5.

was comparable between 9-month-old WT and 5XFAD mice (Figure S2A). Furthermore, immunofluorescent staining showed that BAD significantly translocated to mitochondria in cortical neurons of 5XFAD mice compared with that in WT mice (Figure 2F). Importantly, the percentage of active Casp-3 positive cortical and hippocampal neurons was increased in 5XFAD mice (13.30 ± 1.02% and 1.57 ± 0.11%, respectively), but was reduced in 5XFAD/*Bad*$^{-/-}$ mice (5.36 ± 0.43% and 0.42 ± 0.09%, respectively) to the basal level of neuronal apoptosis triggered by environmental cues such as aging (Hou et al., 2019) in WT mice (3.74 ± 0.36% and 0.36 ± 0.15%, respectively) (Figures 2G, S2B, and S2C), suggesting that *Bad* loss blocked increased Casp-3 activation in cortical and hippocampal neurons of 5XFAD mice. Similar results were obtained in Casp-9 activation, one of the specific initiator caspases in apoptosis, under the same conditions (Figure S3). These results demonstrate that BAD is essential in mediating pathological neuron apoptosis in 5XFAD mice.

We wondered whether BAD is also involved in neuronal necroptosis or pyroptosis in AD. MLKL dimerization, indicative of necroptosis activation in neurons, was significantly increased in brain extracts of 5XFAD mice as previously reported (Caccamo et al., 2017); however, it was not affected by *Bad* loss (Figure S4). *Bad* loss did not affect activation of caspase-1 (Casp-1), indicative of activation of pyroptosis in cortical neurons, as analyzed by immunofluorescent staining (Figure S5). Thus, it is unlikely that BAD affects neuronal necroptosis and pyroptosis in 5XFAD mice. This notion is further supported by the observations that *Bad* loss significantly reduced, but not completely blocked, neurodegeneration and neuronal loss in 5XFAD mice (Figures 2A–2D).

Impaired neurotrophic factor-mediated Akt activation results in increased BAD pro-apoptotic activity in neurons of Alzheimer's disease

To identify possible mechanisms underlying increased BAD pro-apoptotic activity in neurons of AD, we compared the activities of BAD upstream kinases. One of the possibilities for increased BAD mitochondrial translocation in the cortical neurons of patients with AD and 5XFAD mice is that activation of IKK was impaired, which would lead to increased BAD pro-apoptotic activity (Yan et al., 2013, 2018). However, immunofluorescent staining revealed that IKK phosphorylation (Ser176/Ser180 for IKKα and Ser177/Ser181 for IKKβ), indicative of IKK activation, remained unchanged in cortical neurons in patients with AD and 5XFAD mice compared with the controls (Figure S6), indicating that increased neuronal BAD pro-apoptotic activity in AD is not due to impaired IKK activation.

Another possibility is that activation of neurotrophic factor-activated BAD protein kinases such as Akt (Datta et al., 1997) was impaired, considering that production of neurotrophic factors is significantly reduced in AD (Peng et al., 2005). Indeed, immunofluorescent staining revealed that Akt phosphorylation at Ser473, indicative of its activation, was significantly decreased in cortical neurons of 5XFAD mice compared with that in WT mice (Figure 3A), in line with a previous report that direct pharmacological activation of Akt suppresses the development of AD in 5XFAD mice (Yi et al., 2018). Similar results were obtained with Akt-mediated BAD Ser136-phosphorylation in cortical neurons of 9-month-old mice (Figure 3B). Importantly, phosphorylation of Akt at S473 and BAD at S99, which is equivalent to murine BAD S136 (Wang et al., 1999), was also significantly reduced in frontal cortical neurons in patients with AD compared with that in the control (Figures 3C and 3D). The impairment of BAD inactivation by Akt is most likely due to the downregulation of neurotrophic factors production in AD (Finkbeiner, 2000). We found that mature BDNF level was decreased, while pro-NGF level was increased, the latter of which is consistent with impaired procession of pro-NGF to matured NGF seen in AD (Bruno et al., 2009), in brain extracts of 5XFAD mice compared with that in WT mice, and the alterations of mature BDNF and pro-NGF levels were restored in 5XFAD/*Bad*$^{-/-}$ mice (Figures 3E and 3F). Similar results were obtained with brain extracts of patients with AD and controls (Figures 3G and 3H). These observations also explain the restoration of Akt activation in cortical neurons of 5XFAD/*Bad*$^{-/-}$ mice (Figure 3A), in which the levels of neurotrophic factors BDNF and NGF were restored (Figures 3E and 3F). Thus, impaired neurotrophic factor-induced Akt

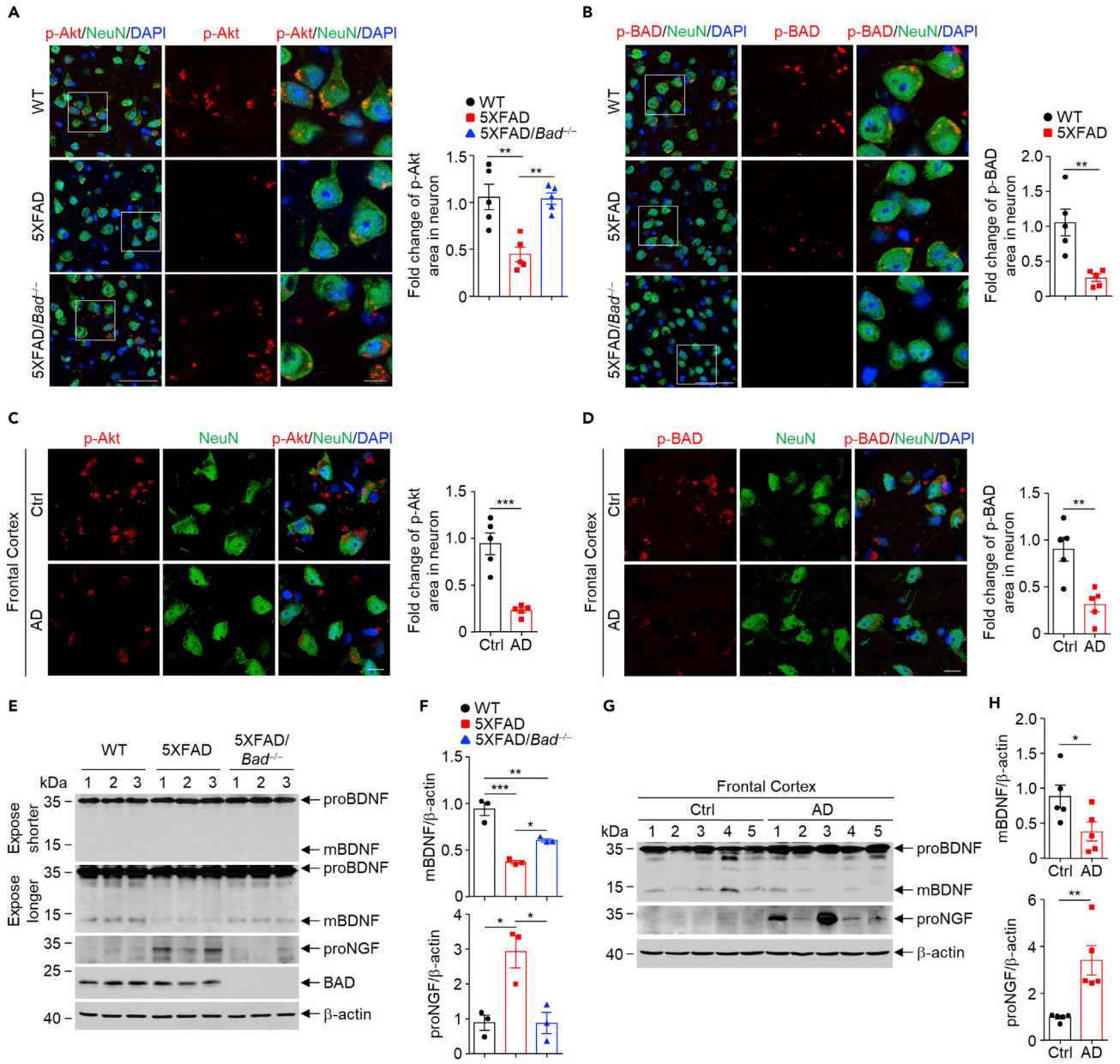

Figure 3. Impaired Akt activation is responsible for increased BAD pro-apoptotic activity in neurons of Alzheimer's disease

(A) Double staining of p-Akt (S473) and NeuN in cortical neurons of 9-month-old WT, 5XFAD and 5XFAD/*Bad*$^{-/-}$ mice. Scale bar, 50 μm; magnified inset, 10 μm. The average area of p-Akt in cortical neurons of 9-month-old mice (n = 5) was quantified. Data were presented as mean ± SEM. **p < 0.01, one-way ANOVA test.

(B) Double staining of p-BAD (S136) and NeuN in cortical neurons of 9-month-old WT, 5XFAD and 5XFAD/*Bad*$^{-/-}$ mice. Scale bar, 50 μm; magnified inset, 10 μm. The average area of p-BAD in cortical neurons of 9-month-old mice (n = 5) was quantified. Data were presented as mean ± SEM. **p < 0.01, student's *t*-test.

(C) Double staining of p-Akt (S473) and NeuN in frontal cortical neurons of patients with Alzheimer's disease and control brains. Scale bar, 10 μm. The average area of p-Akt in frontal cortical neurons of human samples (n = 5) was quantified. Data were presented as mean ± SEM. ***p < 0.001, student's *t*-test.

(D) Double staining of p-BAD (S99) and NeuN in frontal cortical neurons of patients with Alzheimer's disease and age-matched control brains. Scale bar, 10 μm. The average area of p-BAD in frontal cortical neurons of human samples (n = 5) was quantified. Data were presented as mean ± SEM. **p < 0.01, student's *t*-test.

(E) Immunoblotting analysis of BDNF and proNGF protein levels in brain extracts of 9-month-old WT, 5XFAD and 5XFAD/*Bad*$^{-/-}$ mice.

(F) Quantification of the ratio of mBDNF and proNGF relative intensity to β-actin in mouse brain extracts (n = 3). Data were presented as mean ± SEM. *p < 0.05, **p < 0.01, ***p < 0.001, one-way ANOVA test.

Figure 3. *Continued*

(G) Immunoblotting analysis of BDNF and proNGF protein levels in frontal cortex of patients with Alzheimer's disease and age-matched control brains.

(H) Quantification of the ratio of mBDNF and proNGF relative intensity to β-actin in frontal cortex (n = 5). Data were presented as mean ± SEM. *p < 0.05, **p < 0.01, student's *t*-test.

See also Figure S6.

activation is responsible, at least in part, for mitochondrial translocation of hypo-phosphorylated BAD and consequent apoptosis of cortical neurons in 5XFAD mice and patients with AD.

Bad loss promotes microglial Aβ clearance in 5XFAD mice

Aβ accumulation is considered as an initiator of AD, resulting in neuroinflammation, neurodegeneration, neuronal death, and ultimately spatial learning and memory deficits (Ashe and Zahs, 2010). Unexpectedly, Aβ plaque number and burden in cortex and hippocampus of the half brain sections and in the half brain section itself were significantly reduced in 6- and 9-month-old 5XFAD/*Bad*$^{-/-}$ mice compared with age-matched 5XFAD mice, respectively (Figures 4A, 4B, S7A, and S7B). Consistently, ELISA analysis revealed significant reduction of both soluble and insoluble $A\beta_{40}$ and $A\beta_{42}$ in brain extracts of 6-month-old 5XFAD/*Bad*$^{-/-}$ mice compared with 5XFAD mice (Figure S7C), suggesting that BAD plays a crucial role in promoting Aβ deposition in 5XFAD mice. The reduction of Aβ plaque deposition in 5XFAD/*Bad*$^{-/-}$ mice could be the result of decreased Aβ production or increased Aβ phagocytosis by microglia. Interestingly, except the reduction of Aβ protein level, there was no significant difference between 6-month-old 5XFAD/*Bad*$^{-/-}$ and 5XFAD mice in terms of the protein levels of amyloid precursor protein (APP), carboxy (C)-terminal fragments (α-CTF and β-CTF), soluble amyloid precursor protein-α (sAPPα) and β-site APP-converting enzyme 1 (BACE1) (Figures S8A and S8B), as well as expression of two major Aβ degradation enzymes neprilysin (NEP) and insulin-degrading enzyme (IDE) (Figures S8C and S8D). These results indicate that *Bad* loss reduces Aβ plaque deposition without significantly affecting Aβ production and procession in 5XFAD mice.

The above observations prompted us to hypothesize that *Bad* loss promotes microglial phagocytosis of Aβ. Confocal microscopy in combination with 3-dimentional (3D)-rendering quantitative analysis showed that plaque-associated cortical microglia with increased soma volume but reduced branching and complexity, the features of pro-inflammatory microglia in 5XFAD mice compared with WT mice (Figures 4C and 4D). Interestingly, *Bad* loss partially restored these pro-inflammatory microglia morphology changes in 5XFAD mice (Figures 4C and 4D). In support of this notion, confocal microscopy imaging showed that the distance between plaque-associated microglia and Aβ plaque was significantly increased in 5XFAD/*Bad*$^{-/-}$ mice compared with that in 5XFAD mice (Figures 4E and 4F), so were plaque-associated microglia with upregulated expression of CD68 (Figure 4G), which is a microglial phagocytosis marker (Yuan et al., 2016). Expression of TREM2, which is required for uptaking Aβ (Zhao et al., 2018), however, in plaque-associated microglia was comparable between 5XFAD and 5XFAD/*Bad*$^{-/-}$ mice (Figures S8E and S8F). These results indicate that *Bad* loss skews microglia toward phagocytic microglia. In support of this notion, Methoxy-X04-positive microglia, in which intraperitoneally administrated fluorescent derivative of Congo red Methoxy-X04 binds Aβ specifically, were significantly increased in 6-month-old 5XFAD/*Bad*$^{-/-}$ mice (26.28 ± 2.35%) compared with 5XFAD mice (15.38 ± 1.73%), as analyzed by flow cytometry (Figures 4H and 4I). Thus, increased plaque-associated phagocytic microglia are responsible, at least in part, for enhanced clearance of Aβ plaques in 5XFAD/*Bad*$^{-/-}$ mice.

BAD promotes activation of microglial NLRP3 inflammasome via ROS- oxidative mtDNA axis

We speculated that *Bad* loss augments microglial phagocytosis of Aβ plaques by inhibiting neuroinflammatory microglia, which could otherwise suppress phagocytic microglia (Heneka et al., 2013, 2015b). Plaque-associated neuroinflammatory microglia were significantly reduced in 6-month-old 5XFAD/*Bad*$^{-/-}$mice compared to that in 5XFAD mice, as analyzed by immunofluorescent staining of Iba1 (Figures 5A and 5B), so were expression of pro-inflammatory cytokines such as TNFα, IL-1β and IL-6 (Figures 5C and 5D). Consistently, neurotoxic A1 astrocytes, which are activated by neuroinflammatory microglia (Liddelow et al., 2017), were significantly reduced in cortex and hippocampus of 6-month-old 5XFAD/*Bad*$^{-/-}$ mice, as detected by anti-C3 antibody (Figures 5E and 5F).

To understand how *Bad* loss inhibits neuroinflammation, we determined the role of BAD in activation of microglial NLRP3 inflammasome in 5XFAD mice. Immunofluorescent staining revealed that mitochondrial translocation of BAD was significantly increased in cortical microglia of 6-month-old 5XFAD mice compared with that in WT mice (Figure 6A). The cleavage of Casp-1, which is mainly expressed in microglia

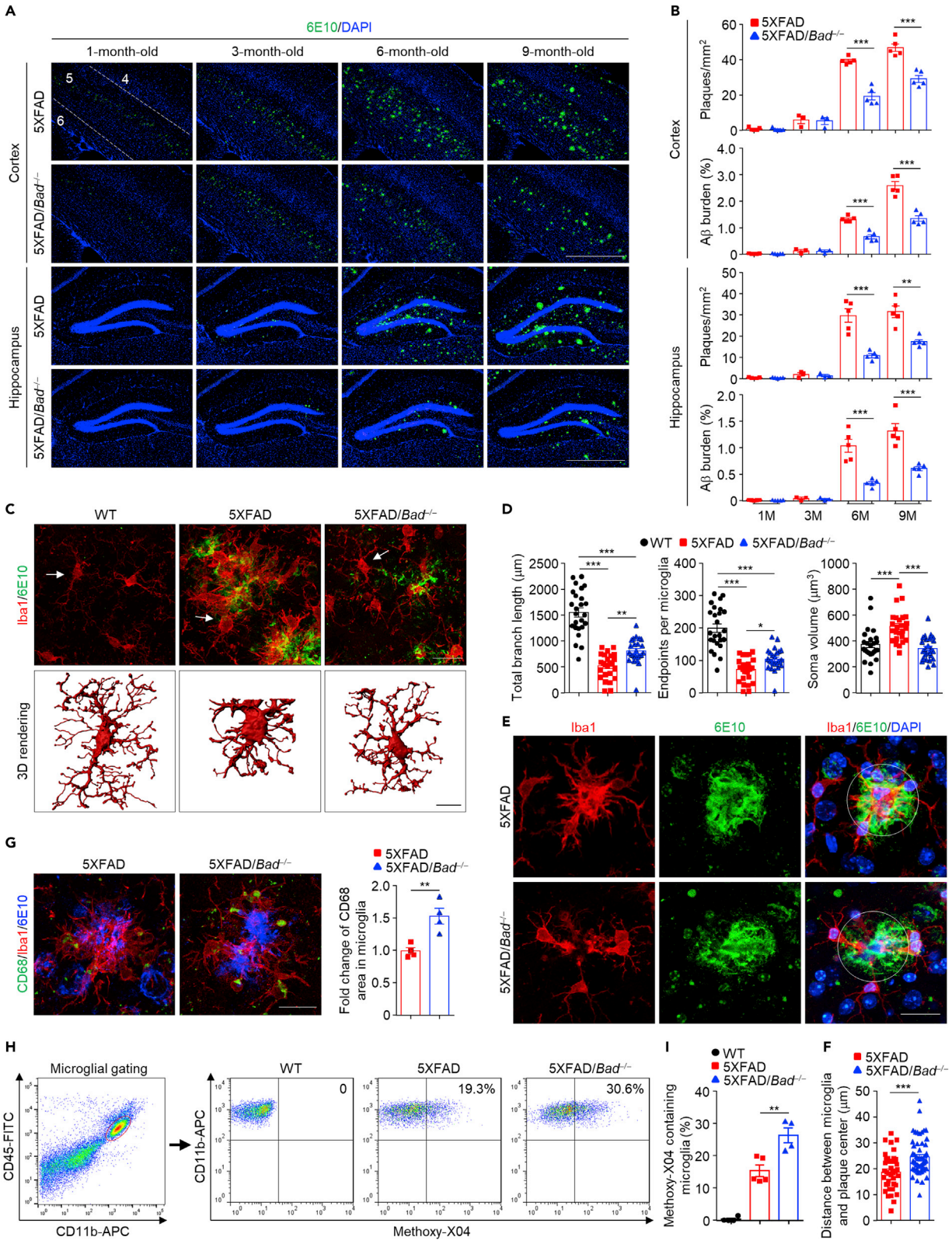
A
6E10/DAPI
1-month-old
3-month-old
6-month-old
9-month-old
Cortex
Hippocampus
5XFAD
5XFAD/Bad-/-
5
4
6
B
5XFAD
5XFAD/Bad-/-
Plaques/mm2
Aβ burden (%)
1M
3M
6M
9M
C
WT
5XFAD
5XFAD/Bad-/-
Iba1/6E10
3D rendering
D
WT
5XFAD
5XFAD/Bad-/-
Total branch length (μm)
Endpoints per microglia
Soma volume (μm3)
E
Iba1
6E10
Iba1/6E10/DAPI
5XFAD
5XFAD/Bad-/-
G
5XFAD
5XFAD/Bad-/-
CD68/Iba1/6E10
Fold change of CD68 area in microglia
H
Microglial gating
CD45-FITC
CD11b-APC
WT
5XFAD
5XFAD/Bad-/-
0
19.3%
30.6%
Methoxy-X04
I
WT
5XFAD
5XFAD/Bad-/-
Methoxy-X04 containing microglia (%)
F
5XFAD
5XFAD/Bad-/-
Distance between microglia and plaque center (μm)

Figure 4. *Bad* loss promotes microglial phagocytosis of Aβ plaques in 5XFAD mice

(A) Aβ plaques in cortex and hippocampus of 5XFAD and 5XFAD/*Bad*$^{-/-}$ mice were detected by immunofluorescent staining with anti-Aβ antibody (6E10) at different time points (1-, 3-, 6- and 9-month-old). Scale bar, 500 μm.

(B) Quantification of the number and burden (% area covered by Aβ plaques) of Aβ plaques in cortex and hippocampus (3-month-old mice, n = 3; 1-, 6- and 9-month-old mice, n = 5). Data were presented as mean ± SEM. **p < 0.01, ***p < 0.001, student's *t*-test.

(C) Representative 3D rendering for plaque-associated microglia in cortex of 6-month-old mice. Scale bar, 20 μm (upper panel), 10 μm (lower panel).

(D) Quantification of microglial total branch length, the number of branch endpoints and the soma volume (n = 25 microglia from 5 mice for each group). Data were presented as mean ± SEM. *p < 0.05, **p < 0.01, ***p < 0.001, one-way ANOVA test.

(E) Representative confocal image of plaque-associated microglia in the cortex of 6-month-old 5XFAD and 5XFAD/*Bad*$^{-/-}$ mice. Scale bar, 20 μm. Circle indicates the edge of Aβ plaque.

(F) Quantification of the distance between microglia and the center of Aβ plaques in 5XFAD (n = 38 microglia from 3 mice) and 5XFAD/*Bad*$^{-/-}$ mice (n = 55 microglia from 3 mice). Data were presented as mean ± SEM. ***p < 0.001, student's *t*-test.

(G) Representative confocal image of CD68 staining in plaque-associated microglia in the cortex of 6-month-old 5XFAD and 5XFAD/*Bad*$^{-/-}$ mice. Scale bar, 20 μm. The average CD68 area in plaque-associated microglia was quantified (n = 4). Data were presented as mean ± SEM. **p < 0.01, student's *t*-test.

(H) Microglial phagocytosis of Aβ (labeled by Methoxy-X04) in 6-month-old 5XFAD and 5XFAD/*Bad*$^{-/-}$ mice were detected by flow cytometry. WT mice served as control.

(I) Quantification of the percentage of Methoxy-X04 containing microglia in 6-month-old WT (n = 4), 5XFAD (n = 5) and 5XFAD/*Bad*$^{-/-}$ (n = 4) mice. Data were presented as mean ± SEM. **p < 0.01, student's *t*-test.

See also Figures S7 and S8.

(Figure S9), was enhanced in brain extracts of 6-month-old 5XFAD mice compared with that in WT mice, but was reduced to the control level in 5XFAD/*Bad*$^{-/-}$ mice (Figure 6B). Consistently, confocal microscopy imaging showed that the percentage of ASC speck-containing microglia, which is a hallmark of NLRP3 inflammasome activation (Stutz et al., 2013), was increased in cortex of 6-month-old 5XFAD mice (39.94 ± 1.71%), as expected (Heneka et al., 2013; Venegas et al., 2017). By contrast, the percentage of ASC speck-containing microglia was significantly reduced in 5XFAD/*Bad*$^{-/-}$ mice (19.74 ± 3.84%) (Figure 6C). More importantly, mitochondrial translocation of BAD was also significantly increased in microglia in frontal cortex of patients with AD compared with that in control brains (Figure 6D), consistent with the increased number of ASC speck-containing microglia (Figure 6E). These results demonstrate that BAD promotes microglial NLRP3 inflammasome activation in both 5XFAD mice and patients with AD.

ROS is a key effector in BAD-dependent mitochondrial apoptotic pathway (Kamata et al., 2005; Yan et al., 2013) and is also involved in activation of NLRP3 inflammasome (Zhou et al., 2011). To determine how BAD activates microglial NLRP3 inflammasome, we measured oxidative mtDNA, which is known to mediate activation of NLRP3 inflammasome by ROS (Shimada et al., 2012; Zhong et al., 2018), rather than ROS itself due to the technical difficulty of directly analyzing ROS accumulation in microglia *in vivo*. Immunofluorescent staining using the antibody against 8-OHdG, a marker of oxidative mtDNA (Shimada et al., 2012), showed that oxidative mtDNA was significantly increased in plaque-associated microglia in cortex of 6-month-old 5XFAD mice compared to cortical microglia in WT mice, but the increase was blunted in 5XFAD/*Bad*$^{-/-}$ mice (Figure 6F), which was consistent with increased oxidative mtDNA level in microglia in frontal cortex of patients with AD compared with that in controls (Figure 6G). These results demonstrate that BAD via ROS-oxidative mtDNA axis, at least in part, promotes NLRP3 inflammasome activation in plaque-associated microglia in both 5XFAD mice and patients with AD.

We also used APP/PS1 mice, another transgenic AD mouse model to test our hypothesis. Unlike 5XFAD mice, APP/PS1 mice have significant neuroinflammation without marked neuronal loss (Caccamo et al., 2017; Jankowsky et al., 2004). To this end, APP/PS1 mice were crossbred *Bad*$^{-/-}$ mice to generate APP/PS1/*Bad*$^{-/-}$ mice. Like aged 5XFAD/*Bad*$^{-/-}$ mice, 9-month-old APP/PS1/*Bad*$^{-/-}$ mice showed reduced number and burden of Aβ plaques in both cortex and hippocampus compared with their age-matched APP/PS1 mice (Figures 7A and 7B). Confocal microscopy revealed significant morphological changes of plaque-associated microglia in the cortex of APP/PS1 mice compared with WT mice, and importantly the morphological changes of these microglia were partially reverted in APP/PS1/*Bad*$^{-/-}$ mice (Figures 7C and 7D), consistent with the results observed in 5XFAD mice. Furthermore, in line with the findings in 5XFAD mice, CD68 expression in plaque-associated microglia was increased (Figures 7E and 7F) but the percentage of ASC speck-containing microglia was decreased in the cortex of APP/PS1/*Bad*$^{-/-}$ mice (36.18 ± 2.86%) compared with that APP/PS1 mice (57.47 ± 3.43%) (Figures 7G and 7H). This result indicates that *Bad* loss also inhibited activation of neuroinflammatory microglia and skewed microglia toward phagocytic state in APP/PS1 mice. APP/PS1 mice exhibited significant poor performance in Y-maze test compared with WT mice, while this memory deficit was rescued in APP/PS1/*Bad*$^{-/-}$ mice (Figure 7I). Taken

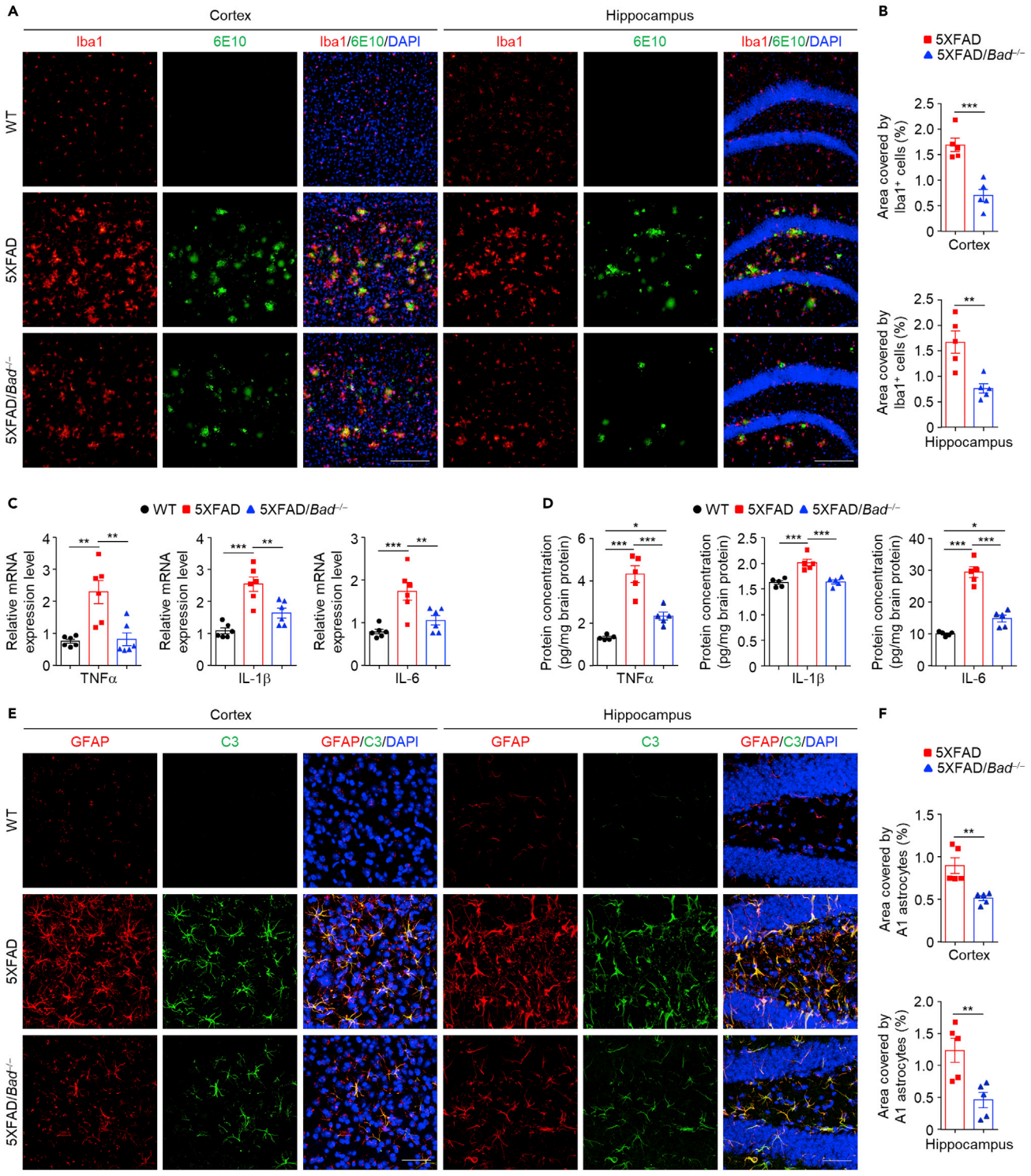

Figure 5. *Bad* loss reduces neuroinflammation and A1 astrocytes activation in 5XFAD mice

(A) Inflammatory microglia in cortex and hippocampus of 6-month-old WT, 5XFAD and 5XFAD/$Bad^{-/-}$ mice were detected by Iba1 and 6E10 double staining. Scale bar, 200 μm.

(B) Quantification of (A) for the area covered by inflammatory microglia in cortex and hippocampus (n = 5). Data were presented as mean ± SEM. **p < 0.01, ***p < 0.001, student's *t*-test.

Figure 5. *Continued*

(C) Relative mRNA expression levels of TNFα, IL-1β and IL-6 in whole brain extracts were detected by real-time qPCR (n = 6). Data were presented as mean ± SEM. **p < 0.01, ***p < 0.001, one-way ANOVA test.

(D) Protein concentration of TNFα, IL-1β and IL-6 in whole brain extracts were detected by ELISA (n = 5). Data were presented as mean ± SEM. *p < 0.05, ***p < 0.001, one-way ANOVA test.

(E) Double immunofluorescent staining of astrocytic pan-active marker GFAP and A1 astrocytic marker C3 in cortex and hippocampus of 6-month-old mice. Scale bar, 50 μm.

(F) Quantification of (E) for the area covered by GFAP and C3 double-positive astrocytes in cortex and hippocampus (n = 5). Data were presented as mean ± SEM. **p < 0.01, student's *t*-test.

together, *Bad* loss reduces neuroinflammation by inhibiting NLRP3 inflammasome activation and reverts the memory deficit in APP/PS1 mice as well.

Viral-mediated deletion of *Bad* in hippocampal neurons reduces neuronal apoptosis and rescues memory deficits in 5XFAD mice

To determine the intrinsic role of BAD in neuronal apoptosis, an AAV9 encoding guide RNA (sg*LacZ* or sg*Bad*) and a reversed SaCas9 that can only be expressed in the presence of Cre, and another AAV9 encoding human synapsin promotor controlled Cre and RFP reporter (Figures 8A and 8B) were injected into dorsal and ventral hippocampus of 4-month-old 5XFAD mice (Figures 8C and 8D). Viral-mediated neuronal deletion of *Bad* resulted in significantly reduced BAD protein level in the hippocampus of 5XFAD mice injected with sg*Bad* guide RNA (Figure 8E). The remaining BAD protein level in hippocampus most likely reflected non-neuronal cells as well as neurons outside the area of AAV infection in the hippocampus. Immunofluorescent staining revealed that AAV-mediated *Bad* loss reduced neuronal apoptosis in the dentate gyrus, as detected by cleaved caspase-3 in neurons (Figure 8F). More importantly, sg*Bad* guide RNA-expressing AAV rescued memory deficits in 5XFAD mice when compared with the control mice, as analyzed by the Y-maze test (Figure 8G). Interestingly, AAV-mediated neuronal *Bad* loss did not significantly affect the Aβ deposition and microglial activation phenotypes in 5XFAD mice (Figure S10). Taken together, these results demonstrate that BAD contributes to neuronal apoptosis intrinsically and suggest that neuronal apoptosis may not be the driver of neuronal inflammation in AD.

DISCUSSION

The pathology of AD is complex, involving major pathological events such as Aβ plaque deposition, neurofibrillary tangle accumulation, neuroinflammation and neuronal loss, thereby leading to spatial learning and memory deficits (Querfurth and LaFerla, 2010; Long and Holtzman, 2019). Despite significant progresses in understanding of the contribution by various pathological events to the development of AD, the key factor that drives AD progression remains elusive. In this report, we demonstrate that BAD mediates neuronal apoptosis and promotes neuroinflammation in both mouse models and patients with AD, thereby identifying BAD as one of the drivers, at least, of the pathogenesis of AD.

BAD is a key regulator of neuronal apoptosis in AD. Previously, it has been reported that neuron death possesses some key features of programmed cell death, i.e., apoptosis, necroptosis, and pyroptosis in mouse models or patients with AD (Caccamo et al., 2017; Cotman and Su, 1996; Kitamura et al., 1998; Su et al., 2002; Tan et al., 2014). However, the genetic link between apoptosis and AD pathology is missing. Our results show that BAD pro-apoptotic activity was increased in frontal cortical and hippocampal tissues, so was Casp-3 activity in frontal cortical neurons in patients with AD. Furthermore, *Bad* loss inhibited neuronal apoptosis and neuronal degeneration, thereby restoring behavioral alteration and cognitive malfunction in 5XFAD mice, which are known to have overt neuronal loss (Eimer and Vassar, 2013; Oakley et al., 2006), indicating that BAD is one of the genetic links between neuronal apoptosis and AD pathology. By contrast, *Bad* loss did not affect neuronal necroptosis or pyroptosis in 5XFAD mice, consistent with the observation that *Bad* loss did not completely block neuronal loss in brain. As expected, *Bad* loss did not have a detectable effect on neurodegeneration and neuronal loss in APP/PS1 mice, which typically do not have detectable neuronal loss due to much slower Aβ accumulation (Yue et al., 2015). Given the fact that *Bad* loss improved spatial learning in APP/PS1 mice, it is possible that BAD may still reduce the much slower and thereby hard to detect neuronal death in APP/PS1 mice (Shi, 2017) as well. Future studies are needed to test this scenario.

The pro-apoptotic activity of BAD is upregulated in AD animal models. Previously, it has been shown that BAD pro-apoptotic activity is typically suppressed by phosphorylation of "regulatory serines" by several protein kinases, including growth factor/survival factor-activated Akt (Datta et al., 1997) and at Ser26 by

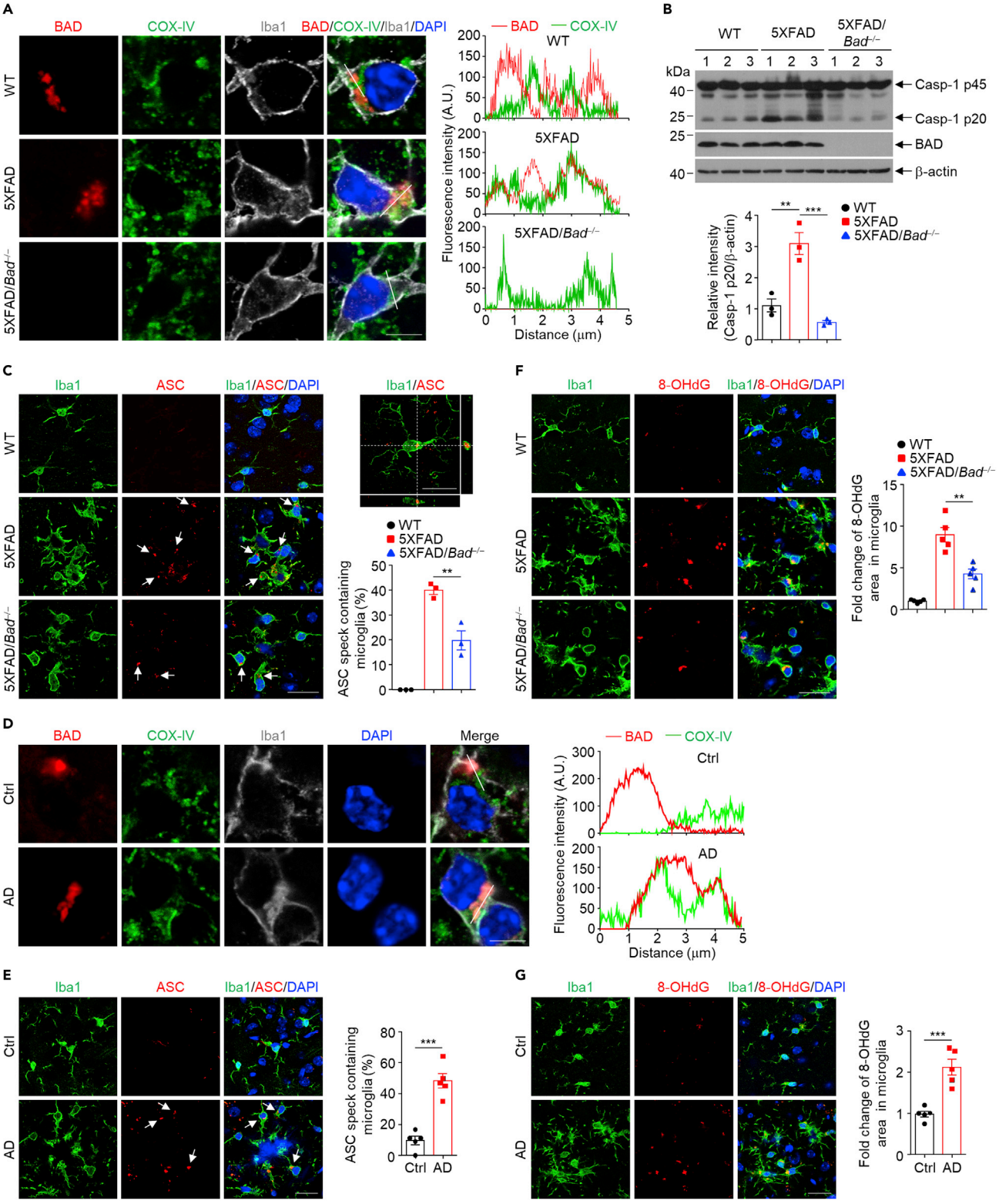

Figure 6. BAD is involved in activation of microglial NLRP3 inflammasome via ROS-oxidative mtDNA axis

(A) Detection of BAD mitochondrial translocation in plaque-associated microglia in the cortex of 6-month-old mice (left panels). Scale bar, 5 μm. The co-localization of BAD and mitochondria was analyzed by the overlap of BAD and COX-IV immunofluorescent signals (right panels).

Figure 6. *Continued*

(B) Immunoblotting analysis of caspase-1 (Casp-1) cleavage in 6-month-old mouse brain extracts. The ratio of Casp-1 p20 relative intensity to β-actin was quantified (n = 3). Data were presented as mean ± SEM. **p < 0.01, ***p < 0.001, one-way ANOVA test.

(C) ASC specks were detected in plaque-associated microglia in the cortex of 6-month-old WT, 5XFAD and 5XFAD/*Bad*$^{-/-}$ mice. Scale bar, 20 μm. The arrows indicate ASC speck-containing microglia. z stack images showed ASC speck was localized inside of microglia. The percentage of ASC speck-containing microglia was quantified (n = 3). Data were presented as mean ± SEM. **p < 0.01, one-way ANOVA test.

(D) Detection of BAD mitochondrial translocation in plaque-associated microglia in the frontal cortex of patients with Alzheimer's disease and age-matched healthy control brains (left panels). Scale bar, 5 μm. The co-localization of BAD with mitochondria was analyzed by the overlap of BAD and COX-IV immunofluorescent signals (right panels).

(E) ASC specks were detected in plaque-associated microglia in the frontal cortex of patients with Alzheimer's disease and control brains. Scale bar, 20 μm. The arrows indicate ASC speck-containing microglia. The percentage of ASC speck-containing microglia was quantified (n = 5). Data were presented as mean ± SEM. ***p < 0.001, student's *t*-test.

(F) Oxidized mitochondrial DNA was detected by immunofluorescent analysis with anti-8-OHdG antibody in plaque-associated microglia in the cortex of 6-month-old WT, 5XFAD and 5XFAD/*Bad*$^{-/-}$ mice. Scale bar, 20 μm. The average area of 8-OHdG in plaque-associated microglia was quantified (n = 5). Data were presented as mean ± SEM. **p < 0.01, one-way ANOVA test.

(G) Oxidized mitochondrial DNA was detected in plaque-associated microglia in the frontal cortex of patients with Alzheimer's disease and age-matched healthy control brains. Scale bar, 20 μm. The average area of 8-OHdG in plaque-associated microglia was quantified (n = 5). Data were presented as mean ± SEM. ***p < 0.001, student's *t*-test.

See also Figure S9.

pro-inflammatory cytokine TNFα-activated IKK(Yan et al., 2013). Our results show that activation of Akt was profoundly reduced in cortical neurons of patients with AD and 5XFAD mice, so was BAD Ser136-phosphorylation, consistent with a recent finding that pharmacological activation of Akt rescues the memory deficits and abnormal synaptic plasticity in 5XFAD mice (Yi et al., 2018). Interestingly, the altered ratio of mBDNF and proNGF, indicative of impaired neuronal survival signaling (Brunet et al., 2001; Nagahara et al., 2009), was significantly restored by *Bad* loss in the brains of 5XFAD mice, suggesting that *Bad* loss not only protects neurons from apoptosis, but also contributes to neuronal survival signaling as survived neuron can produce neurotrophic factors. By contrast, activation of IKK remained unchanged, indicating that upregulation of neuronal BAD pro-apoptotic activity is not the result of downregulation of TNFα-activated IKK, consistent with the fact that the AD induces chronic inflammation in brain (Heneka et al., 2015a). It appears that impaired neurotrophic factors-mediated Akt activation is responsible, at least in part, for upregulation of BAD pro-apoptotic activity in neurons of patients with AD and 5XFAD mouse model.

Our finding that the pro-apoptotic protein BAD has a crucial role in AD pathology is consistent with previous reports regarding the role of neuronal apoptosis in AD (Ghosal et al., 2009; Liddelow et al., 2017; Zhao et al., 2015). However, the pro-apoptotic activity of BAD appears to be selectively regulated, as described above. TNFα is known to involve in AD via promoting neuroinflammation and neuronal death (He et al., 2007) and inflammatory microglia secreted TNFα contributes to neuronal apoptosis via activating neurotoxic A1 astrocytes in AD (Liddelow et al., 2017). However, the increased BAD pro-apoptotic activity in neurons in AD may not result from impaired TNFα-induced IKK activation (Figure S6; see above). Although mice overexpressing APP intracellular domain (AICD) exhibit AD-like pathologies (Ghosal et al., 2009). AICD contributes to neuronal loss via ER stress or p53-mediated apoptotic pathway (Kogel et al., 2012; Ozaki et al., 2006). Thus, it is less likely that AICD is regulated by *Bad* loss. On the other hand, appoptosin has been identified as a novel pro-apoptotic protein in mitochondria-mediated and caspase-dependent intrinsic apoptotic pathway during neuronal death and neurodegeneration (Zhang et al., 2012). Increased protein level of appoptosin has been observed in frontal cortical tissues of AD patients and appoptosin-mediated caspase cleavage of tau aggravates tau pathology (Zhao et al., 2015). Although overexpression of appoptosin does not affect the protein level or phosphorylation of BAD (Zhang et al., 2012), mitochondrial translocation of BAD enhances the pro-apoptotic activity of BAX (Yang et al., 1995), which is upstream of appoptosin-mediated apoptotic pathway. Thus, BAD may act upstream of appoptosin-mediated apoptosis.

BAD skews the polarization of microglia toward to neuroinflammatory microglia in AD. Previously, it has been reported that although Aβ plaques can be cleaned by phagocytic microglia, gradual accumulation of Aβ plaques during the development of AD activates pro-inflammatory microglia via activation of NLRP3 inflammasome (Heneka et al., 2013), subsequent neuroinflammation and A1 astrocytes activation (Liddelow et al., 2017) that suppress phagocytic microglia (Tejera et al., 2019), thereby providing a feedforward feedback on Aβ plaque deposition and AD pathology (Estus et al., 1997; LaFerla et al., 1995; Toshiyuki Nakagawa et al., 2000; Urbanc et al., 2002). Our results show that increased BAD pro-apoptotic activity,

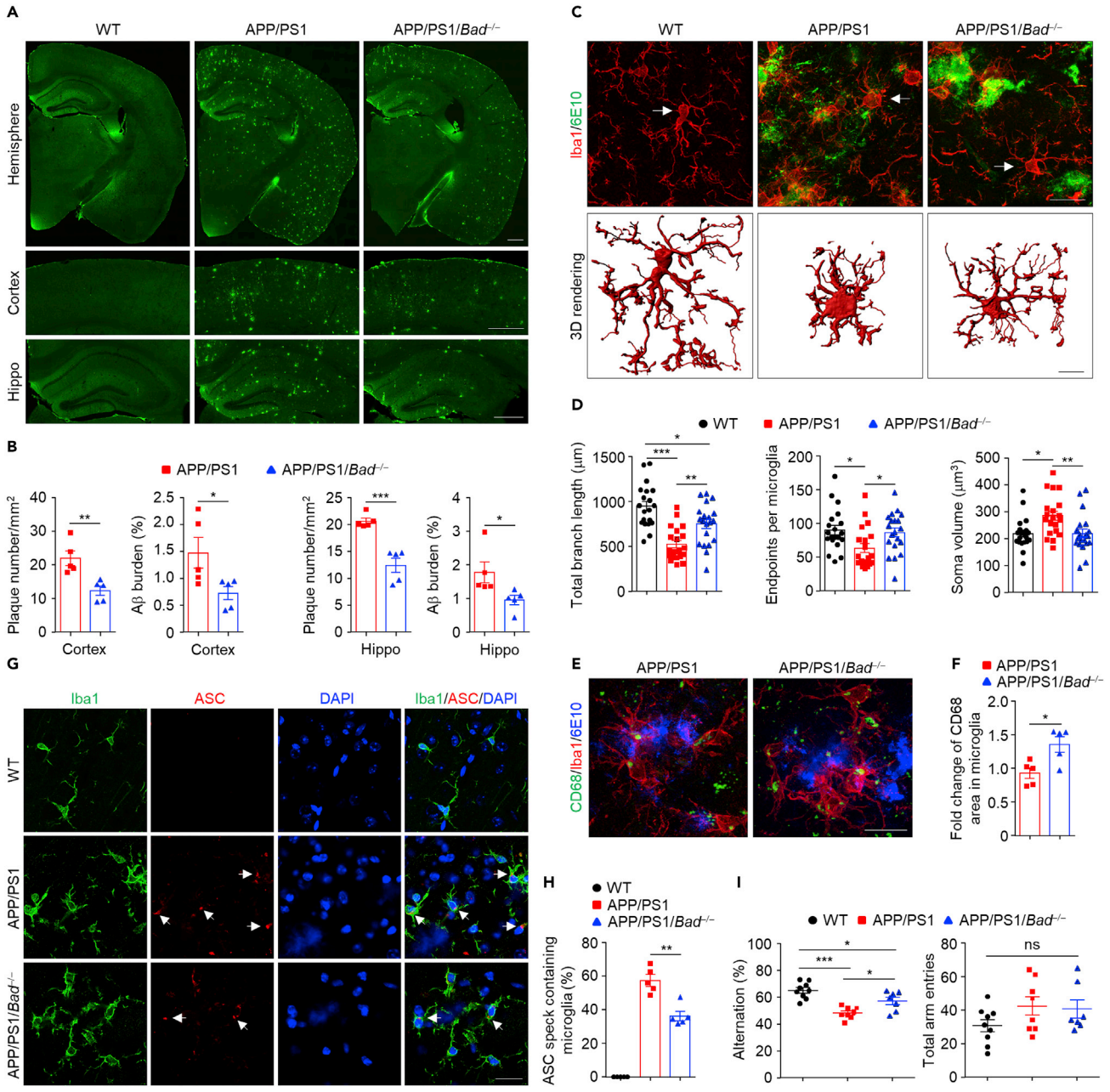

Figure 7. *Bad* loss inhibits Aβ deposition, neuroinflammation and memory deficits in APP/PS1 mice

(A) Aβ plaques in half-brain slices of 9-month-old WT, APP/PS1 and APP/PS1/*Bad*$^{-/-}$ mice were detected by immunofluorescent staining with anti-Aβ antibody (6E10). Scale bar, 500 μm.

(B) Quantification of the number and burden of Aβ plaques in the cortex and hippocampus of 9-month-old APP/PS1 and APP/PS1/*Bad*$^{-/-}$ mice (n = 5). Data were presented as mean ± SEM. *p < 0.05, **p < 0.01, ***p < 0.001, student's *t*-test.

(C) Representative 3D rendering for plaque-associated microglia in the cortex of 9-month-old WT, APP/PS1 and APP/PS1/*Bad*$^{-/-}$ mice. Scale bar, 20 μm (upper panel), 10 μm (lower panel).

(D) Quantification of microglial total branch length, the number of branch endpoints and the soma volume (n = 20, microglia from 5 mice for each group). Data were presented as mean ± SEM. *p < 0.05, **p < 0.01, ***p < 0.001, one-way ANOVA test.

(E) Representative confocal image of CD68 immunofluorescent staining in plaque-associated microglia in the cortex of 9-month-old APP/PS1 and APP/PS1/*Bad*$^{-/-}$ mice. Scale bar, 20 μm.

(F) Quantification of the average CD68 area in plaque-associated microglia in 9-month-old APP/PS1 and APP/PS1/*Bad*$^{-/-}$ mice (n = 5). Data were presented as mean ± SEM. *p < 0.05, student's *t*-test.

Figure 7. *Continued*

(G) ASC specks were detected in plaque-associated microglia in the cortex of 9-month-old WT, APP/PS1 and APP/PS1/*Bad*$^{-/-}$ mice. Scale bar, 20 μm. The arrows indicate ASC speck-containing microglia.

(H) Quantification of the percentage of ASC speck-containing microglia in 9-month-old mice (n = 5). Data were presented as mean ± SEM. **p < 0.01, one-way ANOVA test.

(I) Spatial memory of 9-month-old WT (n = 9), APP/PS1 (n = 8), APP/PS1/*Bad*$^{-/-}$ (n = 7) mice were tested by spontaneous alternation Y-maze test. Data were presented as mean ± SEM. *p < 0.05, ***p < 0.001, one-way ANOVA test.

most likely due to inactivation of Akt, in Aβ plaque-associated microglia, most likely intrinsically, promote microglial NLRP3 inflammasome activation via ROS-oxidative mtDNA axis in Aβ plaque-associated microglia in 5XFAD and APP/PS1 mice, as well as in patients with AD. In addition, BAD contributes to Aβ deposition by suppressing microglial phagocytosis of Aβ. Our finding is consistent with a previous report that in cultured microglia Aβ induced BAD pro-apoptotic activity (Shang et al., 2012), though it was puzzled that under the same conditions Aβ activated Akt, one of the major protein kinases that inactivate BAD. Thus, BAD appears to skew the polarization of microglia toward pro-inflammatory microglia, thereby contributing to suppression of the clearance of Aβ plaques by phagocytic microglia and promotion of Aβ-induced neuronal death.

The identification of BAD orchestrating neuronal apoptosis, neuroinflammation and Aβ plaque accumulation has important pathology significance and clinic relevance. Our results show that BAD contributes to neuronal apoptosis in patients with AD, as its pro-apoptotic activity is significantly increased in frontal cortical neurons, accompanying with impaired neurotrophic factor-activated Akt signaling pathway that otherwise inactivates BAD, consistent with the observation that BAD is responsible for neuronal apoptosis and behavior and cognitive functions in 5XFAD and APP/PS1 mice. Furthermore, BAD promotes microglial NLRP3 activation and neuroinflammation in patients with Alzheimer's disease, as BAD pro-apoptotic activity is increased in microglia, accompany with increased ASC speck-containing microglia and oxidative mtDNA level, again consistent with the observation that BAD is responsible for microglial NLRP3 inflammasome activation via the ROS-oxidative mtDNA axis in 5XFAD mice. Thus, BAD may affect spatial learning and memory directly by mediating neuronal apoptosis and indirectly by promoting neuroinflammation that suppresses microglial phagocytosis of Aβ plaques and reinforces neuronal apoptosis. Despite extensive basic and clinic researches focused on targeting Aβ and tau proteins for decades (Cummings et al., 2018; Godyn et al., 2016), AD remains to be a deadly disease with neither a cure, nor effective therapies (Association, 2019). Although therapeutically preventing or slowing down neuronal death has been hindered by the poorly understanding of the mechanisms and molecular targets underlying neuronal death, selectively targeting the key regulator in neuronal death, e.g., the pro-apoptotic molecule BAD, may provide a therapeutic strategy in treatment of AD, as viral-mediated *Bad* loss in hippocampal neurons can reduce neuronal apoptosis and revert memory deficits in 5XFAD mice. Future studies are needed to test this hypothesis.

Limitations of the study

Although our study demonstrated that BAD contributes to neuronal apoptosis, Aβ deposition and neuroinflammation in the pathogenesis of AD, we cannot precisely distinguish the intrinsic and extrinsic roles of BAD in neurons and microglia with the conventional *Bad*-deficient AD murine models. Neuron- or microglia-specific *Bad*-deficient AD murine models are required to address this question. In addition, although our *in vivo* data demonstrated that *Bad* loss impairs activation of microglial NLRP3 inflammasome, the mechanism by which BAD promotes microglial NLRP3 inflammasome activation has yet to be elucidated in the future studies.

STAR★METHODS

Detailed methods are provided in the online version of this paper and include the following:

- KEY RESOURCES TABLE
- RESOURCE AVAILABILITY
  - Lead contact
  - Materials availability
  - Data and code availability
- EXPERIMENTAL MODEL AND SUBJECT DETAILS
  - Mice

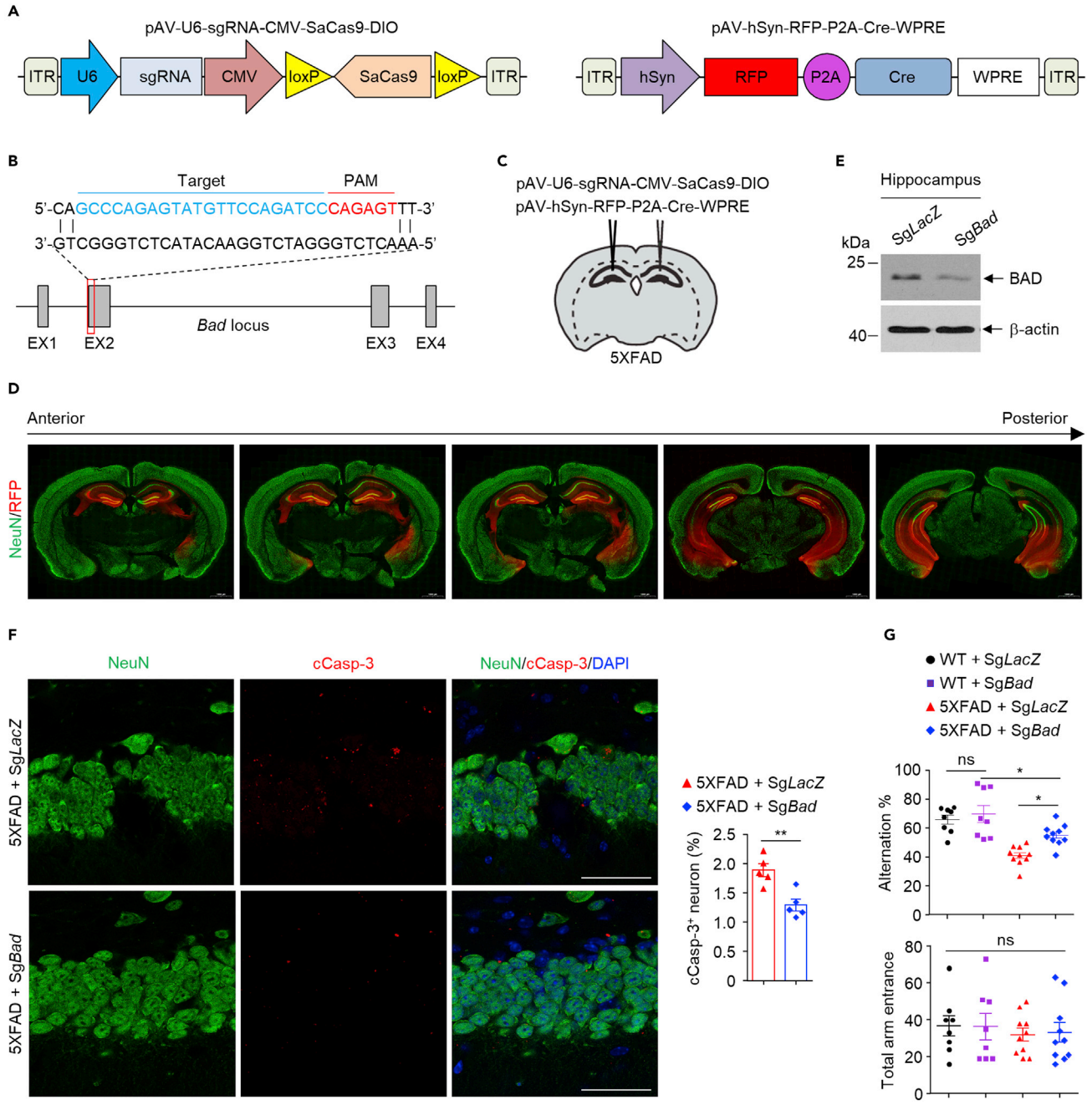

Figure 8. AAV-mediated *Bad* loss reduces neuronal apoptosis and memory deficits in 5XFAD mice

(A) Structures of AAV expression vectors.

(B) Graphical representation of the mouse *Bad* locus showing SaCas9 target location. Targeted genomic locus was indicated in blue and PAM sequence was marked in red.

(C) Strategy of AAV injection in hippocampus of 5XFAD mice.

(D) RFP expression pattern in hippocampus from anterior to posterior after AAV injection. Scale bar, 1000 μm.

(E) Immunoblotting analysis of BAD protein expression in hippocampus after AAV injection, mice injected with pAV-hSyn-RFP-P2A-Cre-WPRE and pAV-U6-sg*LacZ*-CMV-SaCas9-DIO served as controls.

(F) Double staining of cCasp-3 and NeuN in dentate gyrus from 6-month-old 5XFAD + Sg*LacZ* and 5XFAD + Sg*Bad* mice. Scale bar, 50 μm. The percentage of cCasp-3 positive neurons in dentate gyrus was quantified (n = 5). Data were presented as mean ± SEM. **p < 0.01, student's *t*-test.

(G) Spatial memory of 6-month-old WT + Sg*LacZ* (n = 8), WT + Sg*Bad* (n = 8), 5XFAD + Sg*LacZ* (n = 10) and 5XFAD + Sg*Bad* (n = 10) mice were tested by spontaneous alternation Y-maze test. The results were presented as mean ± SEM. *p < 0.05, one-way ANOVA test.

See also Figure S10.

SUPPLEMENTAL INFORMATION

Supplemental information can be found online at https://doi.org/10.1016/j.isci.2021.102942.

ACKNOWLEDGMENTS

We would like to thank Drs. Xiaoxi Zhuang and Gopal Thinakaran for the discussion and advice. This work was supported partially by National Institutes of Health grants (GM103868 and R35 GM122457 to A.L.; CA195526 to J.X.), MOST grants (2016YFE0130500 to X.C.; 2019YFA0801402, 2018YFA0800100, 2018YFA0108003 and 2017YFA0102700 to N.J.), National Key Research and Development Program of China (2016YFC0905900 to B.S.) and National Natural Science Foundation of China (31471077 to X.C.; 31630043 to N.J.; 31430026 and 91329301 to A.L.).

AUTHOR CONTRIBUTIONS

L.Z. performed the experiments, analyzed data, and wrote the manuscript; J.L., X.Z., H.X., Y.Q., X.Y., J.Y., J.X and B.S. contributed to experiment performance, data generation, reagents or results discussion; S.S.S. contributed to the results discussion and manuscript writing; Y.H.J. contributed to obtaining the human tissue; X.C. involved in the supervision of the work by X.Z.; N.J. designed the experiments and analyzed data; A.L. designed the project and experiments, analyzed data and wrote the manuscript.

DECLARATION OF INTERESTS

The authors declare no competing interests.

Received: March 16, 2021
Revised: July 7, 2021
Accepted: July 30, 2021
Published: September 24, 2021

REFERENCES

Ashe, K.H., and Zahs, K.R. (2010). Probing the biology of Alzheimer's disease in mice. Neuron *66*, 631–645.

Association,A.s.(2019).2019Alzheimer'sdisease factsandfigures.Alzheimer'sDemen.*15*,321–387.

Avelina, T., Eva, L., and Isidro, F. (1998). Bcl-2 and Bax protein expression in Alzheimer's disease. Acta Neuropathol. *95*, 407–412.

Biswas, S.C., Shi, Y., Vonsattel, J.-P.G., Leung, C.L., Troy, C.M., and Greene, L.A. (2007). Bim is elevated in Alzheimer's disease neurons and is required for β-amyloid-induced neuronal apoptosis. J. Neurosci. *27*, 893–900.

Brunet, A., Datta, S.R., and Greenberg, M.E. (2001). Transcription-dependent and-independent control of neuronal survival by the PI3K–Akt signaling pathway. Curr.Opin.Neurobiol. *11*, 297–305.

Bruno, M.A., Leon, W.C., Fragoso, G., Mushynski, W.E., Almazan, G., and Cuello, A.C. (2009). Amyloid β-induced nerve growth factor dysmetabolism in Alzheimer disease. J. Neuropathol. Exp. Neurol. *68*, 857–869.

Caccamo, A., Branca, C., Piras, I.S., Ferreira, E., Huentelman, M.J., Liang, W.S., Readhead, B., Dudley, J.T., Spangenberg, E.E., Green, K.N., et al. (2017). Necroptosis activation in Alzheimer's disease. Nat. Neurosci. *20*, 1236–1246.

Cai, Z., Jitkaew, S., Zhao, J., Chiang, H.C., Choksi, S., Liu, J., Ward, Y., Wu, L.G., and Liu, Z.G. (2014). Plasma membrane translocation of trimerized MLKL protein is required for TNF-induced necroptosis. Nat.Cell Biol. *16*, 55–65.

Cao, X., Cui, Z., Feng, R., Tang, Y.P., Qin, Z., Mei, B., and Tsien, J.Z. (2007). Maintenance of superior learning and memory function in NR2B transgenic mice during ageing. Eur. J. Neurosci. *25*, 1815–1822.

Cotman, C.W., and Su, J.H. (1996). Mechanisms of neuronal death in alzheimer's disease. Brain Pathol. *6*, 493–506.

Crews, L., and Masliah, E. (2010). Molecular mechanisms of neurodegeneration in Alzheimer's disease. Hum. Mol. Genet. *19*, R12–R20.

Cummings, J., Lee, G., Ritter, A., and Zhong, K. (2018). Alzheimer's disease drug development pipeline: 2018. Alzheimers Dement.(N Y) *4*, 195–214.

Danial, N.N. (2008). BAD: undertaker by night, candyman by day. Oncogene *27* (*Suppl 1*), S53–S70.

Datta, S.R., Dudek, H., Tao, X., Masters, S., Fu, H., Gotoh, Y., and Greenberg, M.E. (1997). Akt phosphorylation of BAD couples survival signals to the cell-intrinsic death machinery. Cell *91*, 231–241.

Eimer, W.A., and Vassar, R. (2013). Neuron loss in the 5XFAD mouse model of Alzheimer's disease correlates with intraneuronal Aβ42 accumulation and Caspase-3 activation. Mol. Neurodegener. *8*, 1–12.

Estus, S., Tucker, H.M., Van Rooyen, C., Wright, S., Brigham, E.F., Wogulis, M., and Rydel, R.E. (1997). Aggregated amyloid-β protein induces cortical neuronal apoptosis and concomitant "apoptotic" pattern of gene induction. J. Neurosci. *17*, 7736–7745.

Feng, J., Meng, C., and Xing, D. (2015). Aβ induces PUMA activation: a new mechanism for Aβ-mediated neuronal apoptosis. Neurobiol. Aging *36*, 789–800.

Finkbeiner, S. (2000). CREB couples neurotrophin signals to survival messages. Neuron *25*, 11–14.

Ghosal, K., Vogt, D.L., Liang, M., Shen, Y., Lamb, B.T., and Pimplikar, S.W. (2009). Alzheimer's disease-like pathological features in transgenic mice expressing the APP intracellular domain. Proc. Natl. Acad. Sci.U S A *106*, 18367–18372.

Godyn, J., Jonczyk, J., Panek, D., and Malawska, B. (2016). Therapeutic strategies for Alzheimer's disease in clinical trials. Pharmacol. Rep. *68*, 127–138.

Halle, A., Hornung, V., Petzold, G.C., Stewart, C.R., Monks, B.G., Reinheckel, T., Fitzgerald, K.A., Latz, E., Moore, K.J., and Golenbock, D.T. (2008). The NALP3 inflammasome is involved in the innate immune response to amyloid-beta. Nat. Immunol. *9*, 857–865.

He, P., Zhong, Z., Lindholm, K., Berning, L., Lee, W., Lemere, C., Staufenbiel, M., Li, R., and Shen, Y. (2007). Deletion of tumor necrosis factor death receptor inhibits amyloid β generation and prevents learning and memory deficits in Alzheimer's mice. J.Cell Biol. *178*, 829–841.

Heneka, M.T., Carson, M.J., El Khoury, J., Landreth, G.E., Brosseron, F., Feinstein, D.L., Jacobs, A.H., Wyss-Coray, T., Vitorica, J., and Ransohoff, R.M. (2015a). Neuroinflammation in Alzheimer's disease. Lancet Neurol. *14*, 388–405.

Heneka, M.T., Golenbock, D.T., and Latz, E. (2015b). Innate immunity in Alzheimer's disease. Nat. Immunol. *16*, 229–236.

Heneka, M.T., Kummer, M.P., Stutz, A., Delekate, A., Schwartz, S., Vieira-Saecker, A., Griep, A., Axt, D., Remus, A., and Tzeng, T.-C. (2013). NLRP3 is activated in Alzheimer's disease and contributes to pathology in APP/PS1 mice. Nature *493*, 674–678.

Hou, Y., Dan, X., Babbar, M., Wei, Y., Hasselbalch, S.G., Croteau, D.L., and Bohr, V.A. (2019). Ageing as a risk factor for neurodegenerative disease. Nat. Rev. Neurol. *15*, 565–581.

Ising, C., Venegas, C., Zhang, S., Scheiblich, H., Schmidt, S.V., Vieira-Saecker, A., Schwartz, S., Albasset, S., McManus, R.M., and Tejera, D. (2019). NLRP3 inflammasome activation drives tau pathology. Nature *575*, 669–673.

Jankowsky, J.L., Fadale, D.J., Anderson, J., Xu, G.M., Gonzales, V., Jenkins, N.A., Copeland, N.G., Lee, M.K., Younkin, L.H., Wagner, S.L., et al. (2004). Mutant presenilins specifically elevate the levels of the 42 residue beta-amyloid peptide in vivo: evidence for augmentation of a 42-specific gamma secretase. Hum. Mol. Genet. *13*, 159–170.

Kamata, H., Honda, S.-i., Maeda, S., Chang, L., Hirata, H., and Karin, M. (2005). Reactive oxygen species promote TNFα-induced death and sustained JNK activation by inhibiting MAP kinase phosphatases. Cell *120*, 649–661.

Kitamura, Y., Shimohama, S., Kamoshima, W., Ota, T., Matsuoka, Y., Nomura, Y., Smith, M.A., Perry, G., Whitehouse, P.J., and Taniguchi, T. (1998). Alteration of proteins regulating apoptosis, Bcl-2, Bcl-x, Bax, Bak, Bad, ICH-1 and CPP32, in alzheimer's disease. Brain Res. *780*, 260–269.

Kogel, D., Concannon, C.G., Muller, T., Konig, H., Bonner, C., Poeschel, S., Chang, S., Egensperger, R., and Prehn, J.H. (2012). The APP intracellular domain (AICD) potentiates ER stress-induced apoptosis. Neurobiol. Aging *33*, 2200–2209.

Kudo, W., Lee, H., Smith, M., Zhu, X., Matsuyama, S., and Lee, H. (2012). Inhibition of Bax protects neuronal cells from oligomeric Aβ neurotoxicity. Cell Death Dis. *3*, e309.

LaFerla, F.M., Tinkle, B.T., Bieberich, C.J., Haudenschild, C.C., and Jay, G. (1995). The Alzheimer's Aβ peptide induces neurodegeneration and apoptotic cell death in transgenic mice. Nat. Genet. *9*, 21–30.

Liddelow, S.A., Guttenplan, K.A., Clarke, L.E., Bennett, F.C., Bohlen, C.J., Schirmer, L., Bennett, M.L., Munch, A.E., Chung, W.S., Peterson, T.C., et al. (2017). Neurotoxic reactive astrocytes are induced by activated microglia. Nature *541*, 481–487.

Liu, S., Liu, Y., Hao, W., Wolf, L., Kiliaan, A.J., Penke, B., Rübe, C.E., Walter, J., Heneka, M.T., and Hartmann, T. (2012). TLR2 is a primary receptor for Alzheimer's amyloid β peptide to trigger neuroinflammatory activation. J. Immunol. *188*, 1098–1107.

Long, J.M., and Holtzman, D.M. (2019). Alzheimer disease: an update on pathobiology and treatment strategies. Cell *179*, 312–339.

Martinon, F., Burns, K., and Tschopp, J. (2002). The inflammasome: a molecular platform triggering activation of inflammatory caspases and processing of proIL-β. Mol.Cell *10*, 417–426.

Nagahara, A.H., Merrill, D.A., Coppola, G., Tsukada, S., Schroeder, B.E., Shaked, G.M., Wang, L., Blesch, A., Kim, A., Conner, J.M., et al. (2009). Neuroprotective effects of brain-derived neurotrophic factor in rodent and primate models of Alzheimer's disease. Nat. Med. *15*, 331–337.

Nicoll, R.A. (2017). A brief history of long-term potentiation. Neuron *93*, 281–290.

Oakley, H., Cole, S.L., Logan, S., Maus, E., Shao, P., Craft, J., Guillozet-Bongaarts, A., Ohno, M., Disterhoft, J., and Van Eldik, L. (2006). Intraneuronal β-amyloid aggregates, neurodegeneration, and neuron loss in transgenic mice with five familial Alzheimer's disease mutations: potential factors in amyloid plaque formation. J. Neurosci. *26*, 10129–10140.

Ohno, M., Sametsky, E.A., Younkin, L.H., Oakley, H., Younkin, S.G., Citron, M., Vassar, R., and Disterhoft, J.F. (2004). BACE1 deficiency rescues memory deficits and cholinergic dysfunction in a mouse model of alzheimer's disease. Neuron *41*, 27–33.

Ozaki, T., Li, Y., Kikuchi, H., Tomita, T., Iwatsubo, T., and Nakagawara, A. (2006). The intracellular domain of the amyloid precursor protein (AICD) enhances the p53-mediated apoptosis. Biochem.Biophys. Res. Commun. *351*, 57–63.

Peng, S., Wuu, J., Mufson, E.J., and Fahnestock, M. (2005). Precursor form of brain-derived neurotrophic factor and mature brain-derived neurotrophic factor are decreased in the pre-clinical stages of Alzheimer's disease. J. Neurochem. *93*, 1412–1421.

Querfurth, H.W., and LaFerla, F.M. (2010). Mechanisms of disease. N. Engl. J. Med. *362*, 329–344.

Rohn, T.T., Vyas, V., Hernandez-Estrada, T., Nichol, K.E., Christie, L.A., and Head, E. (2008). Lack of pathology in a triple transgenic mouse model of alzheimer's disease after overexpression of the anti-apoptotic protein Bcl-2. J. Neurosci. *28*, 3051–3059.

Schägger, H. (2006). Tricine–SDS-PAGE. Nat. Protoc. *1*, 16–22.

Shang, Y.C., Chong, Z.Z., Wang, S., and Maiese, K. (2012). Prevention of β-amyloid degeneration of microglia by erythropoietin depends on Wnt1, the PI 3-K/mTOR pathway, Bad, and Bcl-xL. Aging (Albany NY) *4*, 187.

Shi, Q. (2017). Complement C3 deficiency protects against neurodegeneration in aged

plaque-rich APPPS1 mice. Sci. Transl.Med. *9*, eaaf6295.

Shimada, K., Crother, T.R., Karlin, J., Dagvadorj, J., Chiba, N., Chen, S., Ramanujan, V.K., Wolf, A.J., Vergnes, L., Ojcius, D.M., et al. (2012). Oxidized mitochondrial DNA activates the NLRP3 inflammasome during apoptosis. Immunity *36*, 401–414.

Stutz, A., Horvath, G.L., Monks, B.G., and Latz, E. (2013). ASC speck formation as a readout for inflammasome activation. Methods Mol. Biol. *1040*, 91–101.

Su, J.H., Kesslak, J.P., Head, E., and Cotman, C.W. (2002). Caspase-cleaved amyloid precursor protein and activated caspase-3 are co-localized in the granules of granulovacuolar degeneration in Alzheimer's disease and Down's syndrome brain. Acta Neuropathol. *104*, 1–6.

Tan, M.S., Tan, L., Jiang, T., Zhu, X.C., Wang, H.F., Jia, C.D., and Yu, J.T. (2014). Amyloid-beta induces NLRP1-dependent neuronal pyroptosis in models of Alzheimer's disease. Cell Death Dis. *5*, e1382.

Tarasoff-Conway, J.M., Carare, R.O., Osorio, R.S., Glodzik, L., Butler, T., Fieremans, E., Axel, L., Rusinek, H., Nicholson, C., Zlokovic, B.V., et al. (2015). Clearance systems in the brain-implications for Alzheimer disease. Nat. Rev. Neurol. *11*, 457–470.

Tejera, D., Mercan, D., Sanchez-Caro, J.M., Hanan, M., Greenberg, D., Soreq, H., Latz, E., Golenbock, D., and Heneka, M.T. (2019). Systemic inflammation impairs microglial Aβ clearance through NLRP3 inflammasome. EMBO J. *38*, e101064.

Toshiyuki Nakagawa, H.Z., Nobuhiro Morishima, En Li, Xu, Jin, Yankner, Bruce A., and Yuan, Junying (2000). Caspase-12 mediates endoplasmic-reticulum-specific apoptosis and cytotoxicity of amyloid-beta. Nature *403*, 98–103.

Urbanc, B., Cruz, L., Le, R., Sanders, J., Ashe, K.H., Duff, K., Stanley, H., Irizarry, M., and Hyman, B. (2002). Neurotoxic effects of thioflavin S-positive amyloid deposits in transgenic mice and Alzheimer's disease. Proc. Natl. Acad. Sci. USA *99*, 13990–13995.

Venegas, C., Kumar, S., Franklin, B.S., Dierkes, T., Brinkschulte, R., Tejera, D., Vieira-Saecker, A., Schwartz, S., Santarelli, F., Kummer, M.P., et al. (2017). Microglia-derived ASC specks cross-seed amyloid-beta in Alzheimer's disease. Nature *552*, 355–361.

Vorhees, C.V., and Williams, M.T. (2006). Morris water maze: procedures for assessing spatial and related forms of learning and memory. Nat. Protoc. *1*, 848–858.

Wang, H.-G., Pathan, N., Ethell, I.M., Krajewski, S., Yamaguchi, Y., Shibasaki, F., McKeon, F., Bobo, T., Franke, T.F., and Reed, J.C. (1999). Ca2+-induced apoptosis through calcineurin dephosphorylation of BAD. Science *284*, 339–343.

Yamanaka, M., Ishikawa, T., Griep, A., Axt, D., Kummer, M.P., and Heneka, M.T. (2012). PPARgamma/RXRalpha-induced and CD36-mediated microglial amyloid-beta phagocytosis results in cognitive improvement in amyloid precursor protein/presenilin 1 mice. J. Neurosci. *32*, 17321–17331.

Yan, J., Xiang, J., Lin, Y., Ma, J., Zhang, J., Zhang, H., Sun, J., Danial, N.N., Liu, J., and Lin, A. (2013). Inactivation of BAD by IKK inhibits TNFα-induced apoptosis independently of NF-κB activation. Cell *152*, 304–315.

Yan, J., Zhang, H., Xiang, J., Zhao, Y., Yuan, X., Sun, B., and Lin, A. (2018). The BH3-only protein BAD mediates TNFalpha cytotoxicity despite concurrent activation of IKK and NF-kappaB in septic shock. Cell Res. *28*, 701–718.

Yang, E., Zha, J., Jockel, J., Boise, L.H., Thompson, C.B., and Korsmeyer, S.J. (1995). Bad, a heterodimeric partner for Bcl-XL and Bcl-2, displaces Bax and promotes cell death. Cell *80*, 285–291.

Yi, J.H., Baek, S.J., Heo, S., Park, H.J., Kwon, H., Lee, S., Jung, J., Park, S.J., Kim, B.C., Lee, Y.C., et al. (2018). Direct pharmacological Akt activation rescues Alzheimer's disease like memory impairments and aberrant synaptic plasticity. Neuropharmacology *128*, 282–292.

Yuan, P., Condello, C., Keene, C.D., Wang, Y., Bird, T.D., Paul, S.M., Luo, W., Colonna, M., Baddeley, D., and Grutzendler, J. (2016). TREM2 haplodeficiency in mice and humans impairs the microglia barrier function leading to decreased amyloid compaction and severe axonal dystrophy. Neuron *90*, 724–739.

Yue, W., Li, Y., Zhang, T., Jiang, M., Qian, Y., Zhang, M., Sheng, N., Feng, S., Tang, K., and Yu, X. (2015). ESC-derived basal forebrain cholinergic neurons ameliorate the cognitive symptoms associated with Alzheimer's disease in mouse models. Stem Cell Rep. *5*, 776–790.

Zhang, H., Zhang, Y.W., Chen, Y., Huang, X., Zhou, F., Wang, W., Xian, B., Zhang, X., Masliah, E., Chen, Q., et al. (2012). Appoptosin is a novel pro-apoptotic protein and mediates cell death in neurodegeneration. J. Neurosci. *32*, 15565–15576.

Zhao, S., Zhao, J., Zhang, T., and Guo, C. (2016). Increased apoptosis in the platelets of patients with Alzheimer's disease and amnestic mild cognitive impairment. Clin. Neurol. Neurosurg. *143*, 46–50.

Zhao, Y., Tseng, I.C., Heyser, C.J., Rockenstein, E., Mante, M., Adame, A., Zheng, Q., Huang, T., Wang, X., Arslan, P.E., et al. (2015). Appoptosin-mediated caspase cleavage of tau contributes to progressive supranuclear palsy pathogenesis. Neuron *87*, 963–975.

Zhao, Y., Wu, X., Li, X., Jiang, L.L., Gui, X., Liu, Y., Sun, Y., Zhu, B., Pina-Crespo, J.C., Zhang, M., et al. (2018). TREM2 is a receptor for beta-amyloid that mediates microglial function. Neuron *97*, 1023–1031 e1027.

Zhong, Z., Liang, S., Sanchez-Lopez, E., He, F., Shalapour, S., Lin, X.J., Wong, J., Ding, S., Seki, E., Schnabl, B., et al. (2018). New mitochondrial DNA synthesis enables NLRP3 inflammasome activation. Nature *560*, 198–203.

Zhou, R., Yazdi, A.S., Menu, P., and Tschopp, J. (2011). A role for mitochondria in NLRP3 inflammasome activation. Nature *469*, 221–225.

STAR★METHODS

KEY RESOURCES TABLE

REAGENT or RESOURCE	SOURCE	IDENTIFIER
Antibodies		
Rabbit anti-BAD	Abcam	Cat# ab32445; RRID:AB_725614
Mouse anti-COX-IV	Abcam	Cat# ab33985; RRID:AB_879754
Rabbit anti-GFAP	Abcam	Cat# ab16997; RRID:AB_443592
Rabbit anti-CD68	Abcam	Cat# ab125212; RRID:AB_10975465
Rabbit anti-BDNF	Abcam	Cat# ab108319; RRID:AB_10862052
Rabbit anti-p-Akt (S473)	Cell Signaling Technology	Cat# 4060; RRID:AB_2315049
Rabbit anti-p-BAD (S136)	Cell Signaling Technology	Cat# 4366; RRID:AB_10547878
Rabbit anti-p-IKKα/β (Ser176/180)	Cell Signaling Technology	Cat# 2697; RRID:AB_2079382
Rabbit anti-BACE	Cell Signaling Technology	Cat# 5606; RRID:AB_1903900
Rabbit anti-BAD	Cell Signaling Technology	Cat# 9292; RRID:AB_331419
Rabbit anti-Cleaved caspase-9	Cell Signaling Technology	Cat# 9509; RRID: AB_2073476
Mouse anti-NGF	Santa Cruz Biotechnology	Cat# sc-365944; RRID:AB_10917399
Mouse anti-α-tubulin	Santa Cruz Biotechnology	Cat# sc-8035; RRID:AB_628408
Mouse anti-Tom20	Santa Cruz Biotechnology	Cat# sc-11415; RRID:AB_2207533
Mouse anti-β-actin	Santa Cruz Biotechnology	Cat# sc-47778; RRID:AB_2714189
Goat anti-C3d	R&D Systems	Cat# AF2655; RRID:AB_2066622
Sheep anti-TREM2	R&D Systems	Cat# AF1729; RRID:AB_354956
Mouse anti-Caspase-1 p20 (mouse)	AdipoGen	Cat# AG-20B-0042; RRID:AB_2490248
Mouse anti-Caspase-1 p20 (human)	AdipoGen	Cat# AG-20B-0048; RRID:AB_2490257
Mouse anti-ASC	Millipore	Cat# 04-147; RRID:AB_1977033
Rabbit anti-Cleaved caspase-3	Millipore	Cat# AB3623; RRID:AB_91556
Guinea pig anti-NeuN	Millipore	Cat# ABN90P; RRID:AB_2341095
Mouse anti-β-amyloid	Covance	Cat# SIG-39320; RRID:AB_662798
Mouse anti-APP C-terminal fragment	Covance	Cat# SIG-39152; RRID:AB_10717336
Rabbit anti-NEP (MME)	ABclonal	Cat# A5664; RRID:AB_2766424
Rabbit anti-IDE	ABclonal	Cat# A1630; RRID:AB_2861723
Mouse anti-human sAPPα	Immuno-Biological Laboratories	Cat# 11088; RRID:AB_494690
Rabbit anti-MLKL	Biorbyt	Cat# orb32399; RRID:AB_10927389
Rabbit anti-8-OHdG	Bioss	Cat# BS-1278R; RRID:AB_10856120
Goat anti-Iba1	Novus Biologicals	Cat# NB100-1028; RRID:AB_521594
Rat anti-mouse/human CD11b-APC	Biolegend	Cat# 101211; RRID:AB_312794
Rat anti-mouse CD45-FITC	Biolegend	Cat# 103107; RRID:AB_312972
Biological Samples		
Frontal cortical samples from AD patients and controls	Duke Kathleen Price Bryan Brain Bank and Biorepository	For patient information, see Table S1
Hippocampal samples from AD patients and controls	Duke Kathleen Price Bryan Brain Bank and Biorepository	For patient information, see Table S1
Chemicals, Peptides, and Recombinant Proteins		
Fluoro-Jade C	Millipore	Cat# AG325
Methoxy-X04	Tocris	Cat# 4920
DNase I	Roche	Cat# 11284932001

(*Continued on next page*)

Continued

REAGENT or RESOURCE	SOURCE	IDENTIFIER
Dispase II	Roche	Cat# 04942078001
Collagenase type IV	Gibco	Cat# 17104019
Percoll	GE Healthcare	Cat# 17089102
Mouse Fc block	BD Bioscience	Cat# 553141
Critical Commercial Assays		
$A\beta_{40}$ Human ELISA Kit	Invitrogen	Cat# KHB3482
Ultrasensitive $A\beta_{42}$ Human ELISA Kit	Invitrogen	Cat# KHB3544
Mouse TNFα Quantikine ELISA kit	R&D Systems	Cat# MTA00B
Mouse IL-1β Quantikine ELISA Kit	R&D Systems	Cat# MLB00C
Mouse IL-6 Quantikine ELISA kit	R&D Systems	Cat# M6000B
Mitochondria Isolation Kit for Tissue	Thermo Fisher Scientific	Cat# 89801
Experimental Models: Organisms/Strains		
Mouse: B6.Cg-Tg(APPSwFlLon,PSEN1*M146L*L286V)6799Vas/Mmjax (5XFAD)	The Jackson Laboratory	Cat# 34848-JAX; RRID:MMRRC_034848-JAX
Mouse: B6.Cg-Tg(APPswe,PSEN1dE9)85Dbo/Mmjax (APP/PS1)	The Jackson Laboratory	Cat# 34832-JAX; RRID:MMRRC_034832-JAX
Mouse: C57BL/6J	The Jackson Laboratory	Cat# JAX:000664; RRID:IMSR_JAX:000664
Mouse: *Bad*$^{-/-}$	Nike N. Danial (Danial, 2008)	N/A
Oligonucleotides		
TNFαqPCR primer, forward (CCAAGGCGCCACATCTCCCT)	Integrated DNA Technologies	N/A
TNFαqPCR primer, reverse (GCTTTCTGTGCTCATGGTGT)	Integrated DNA Technologies	N/A
IL-1βqPCR primer, forward (GAAGAAGAGCCCATCCTCTG)	Integrated DNA Technologies	N/A
IL-1βqPCR primer, reverse (TCATCTCGGAGCCTGTAGTG)	Integrated DNA Technologies	N/A
IL-6 qPCR primer, forward (TAGTCCTTCCTACCCCAATTTCC)	Integrated DNA Technologies	N/A
IL-6 qPCR primer, reverse (TTGGTCCTTAGCCACTCCTTC)	Integrated DNA Technologies	N/A
Software and Algorithms		
Fiji-ImageJ	National Institute of Health	https://imagej.net/Fiji; RRID:SCR_003070
GraphPad Prism 6	GraphPad	https://www.graphpad.com/scientific-software/prism/; RRID:SCR_002798
FlowJo v10.4	Tree Star	https://www.flowjo.com/solutions/flowjo; RRID:SCR_008520
Imaris	Bitplane	http://www.bitplane.com/imaris/imaris; RRID:SCR_007370
Other		
BX51 microscope	Olympus	N/A
TCS SP5 two-photon confocal microscope	Leica	N/A
TCS SP8 confocal microscope	Leica	N/A
Celesta flow cytometer	BD Biosciences	N/A
LSRFortessa flow cytometer	BD Biosciences	N/A

RESOURCE AVAILABILITY

Lead contact

Further information and requests for resources and reagents should be directed to and will be fulfilled by the lead contact, Anning Lin (anninglin@nju.edu.cn).

Materials availability

This study did not generate new unique reagents.

Data and code availability

- Data reported in this paper will be shared by the lead contact upon request.
- This paper does not report original code.
- Any additional information required to reanalyze the data reported in this paper is available from the lead contact upon request.

EXPERIMENTAL MODEL AND SUBJECT DETAILS

Mice

5XFAD/*Bad*$^{-/-}$ mice and APP/PS1/*Bad*$^{-/-}$ mice were generated by crossbreeding *Bad*$^{-/-}$ mice (Yan et al., 2018) with 5XFAD mice and APP/PS1 mice (Yue et al., 2015), respectively. Detailed information of the mice was indicated in key resources table. Male mice were used for all experiments. Age of the mice and sample size (n) were mentioned in figure legend for each experiment. For behavioral test, electrophysiological analysis and microscopic analysis of immunofluorescent staining, the experimenters were blinded to genotype. Animal protocols were reviewed and approved by the Institutional Animal Care and Use Committee in Shanghai Institute of Biochemistry and Cell Biology or the University of Chicago. All experiments conform to the relevant regulatory standards.

Human brain samples

Frontal cortex and hippocampus brain tissues of patients with Alzheimer's disease and age-matched controls without neurological disease were obtained from Duke Kathleen Price Bryan Brain Bank and Biorepository, and informed consent was obtained from all subjects. The information of the patients was indicated in Table S1. This study was approved by the Institutional Review Board at the University of Chicago.

METHODS DETAILS

Behavioral test

For Morris water maze test, a 12-cm diameter round platform was placed 1 cm underneath the water surface, which was made opaque using nontoxic white paint at the center of a given quadrant in a circle tank (120 cm diameter and 50 cm high). Invisible platform training was carried out for 6 consecutive days, and 4 trials were performed for each day. For each trial, mice were released from the wall of water tank and allowed to search and stand on the platform for 20 s within 60 s. Mice were guided to the platform and allowed to stand on the platform for 20 s if they failed to find the platform within 60 s. The starting quadrant from where mice were released and the sequence of four quadrants were randomly chosen for each training session. Performances of testing mice were recorded by a video camera (Noldus system). 24 hr after completion of the training stage, the platform in the tank was removed and the task performances of each mouse were recorded for 60 s for probe test. Times that mouse crossing the region where the platform was placed and time spent in target quadrant was analyzed as previously described (Vorhees and Williams, 2006).

For spontaneous alternation Y-maze test, there was no training, reward, or punishment when assessing the spatial memory of the mice, which is dependent upon the hippocampus (Ohno et al., 2004). The Y maze equipment has three arms separated by 120 degrees, and each arm is 35 cm long, 8 cm high and 5 cm wide. During the Y-maze test, each mouse was allowed to explore the Y-maze freely from the center of maze for 8 minutes. The total arm entrances and sequence were recorded for analysis. A completed entrance was recorded only when hind paws of testing mouse had been placed into the arm completely. The alternation percentage was calculated using the following formula:

$$Alternation\% = \frac{Number\ of\ triads\ containing\ entrances\ into\ three\ arms}{Total\ arm\ entrances - 2} \times 100\%$$

Electrophysiology

Hippocampal recordings procedures were performed to compare the LTP (Cao et al., 2007). Briefly, 8-month-old WT, 5XFAD and 5XFAD/$Bad^{-/-}$ mice were deeply anaesthetized. Mouse brain was quickly taken out and put into modified artificial cerebrospinal fluid under cold (4°C) and oxygenated (95% O_2, 5% CO_2) condition. Whole-brain coronal sections (370 μm) containing the hippocampus were cut and then placed in an incubation chamber with normal artificial cerebrospinal fluid for 60 min under oxygenated condition. After incubation, a unipolar tungsten stimulating electrode was placed in CA3 region to deliver electro-stimuli and a 3 MΩ glass microelectrode was positioned in the CA1 region to record extracellular field potentials. Test responses were elicited at 0.033 Hz. After obtaining a stable baseline response for at least 15 min, LTP was induced by three trains of theta burst stimulation.

Brain samples preparation

Mice were perfused with ice-cold PBS after deep anesthesia. Right-brain hemispheres were fixed in 4% PFA for 24 hr and then placed sequentially in 15% and 30% sucrose overnight to dehydrate. Dehydrated hemispheres were stored at −80°C for further frozen section. Dehydrated right-brain hemispheres were sectioned for serial 30 μm coronal sections using a vibratome (Leica) and stored in anti-freezing solution (0.02 M NaH_2PO_4, 0.08 M Na_2HPO_4, 1% PVP-40, 30% sucrose and 30% ethylene glycol) at -20°C before staining. Left-brain hemispheres were flash frozen in liquid nitrogen for immunoblotting analysis, cytosol/mitochondria fractionation, ELISA or mRNA expression analysis.

Cytosol/mitochondria fractionation

BAD mitochondrial translocation in human or mouse brain samples was analyzed by cytosol/mitochondria fractionation using Mitochondria Isolation Kit for Tissue (#89801, Thermo Fisher Scientific). Tom20 was used as a mitochondrial marker and α-tubulin or β-actin was used as the marker of cytosol.

Fluoro-Jade C staining

Neurodegeneration was analyzed by Fluoro-Jade C (AG325, Millipore) staining according to the manufacturer's instructions with modification. Briefly, free-floating sections were washed with PBS 5 times 5 min each time to remove anti-freezing solution and then pre-treated sequentially in 80% ethanol containing 1% NaOH for 5 min, 70% ethanol for 2 min, 50% ethanol for 2 min, 30% ethanol for 2 min, 10% ethanol for 2 min, ddH_2O twice 2 min each time, 0.06% potassium permanganate for 10 min and ddH_2O twice 2 min each time. After pre-treatment, brain sections were stained with 0.0001% FJC working solution containing DAPI (Sigma) dye for 20 min and then washed with ddH_2O for 3 times to remove extra FJC solution. Brain sections were finally recovered in PBS and mounted on slides.

Nissl staining

Neuronal density in cortical layer 5 and subiculum were detected by Nissl staining using Cresyl Violet (Eimer and Vassar, 2013). Briefly, brain sections were thoroughly washed with PBS to remove anti-freezing solution, mounted on charged slides and allowed to dry overnight. Sections were first rinsed in ddH_2O and then stained with 0.5% Cresyl Violet for 10 min. Sections were then rinsed in ddH_2O and dehydrated in 70% ethanol for 5 min, 95% ethanol for 1 min, and de-stained in 95% ethanol containing 0.7% glacial acetic acid for 1 min. Sections were sequentially placed in 100% ethanol twice 2 min each time, ethanol: xylene (1: 1) for 5 minutes, xylene for 5 min and finally mounted.

Immunohistochemistry (mouse)

Mouse brain sections were washed with PBS to thoroughly remove anti-freezing solution and permeabilized in 0.3% Triton X-100 in PBS for 30 minutes. Sections were incubated with primary antibodies overnight at 4°C after incubation in blocking buffer (3% BSA in PBS) for 1 hour. Before staining with anti-p-BAD (S136), primary antibody solution (1:200) was incubated twice with membranes from SDS-PAGE loaded with $Bad^{-/-}$ mouse brain extracts overnight to eliminate non-specific bindings and immunoblotting analysis was performed to confirm the elimination of non-specific bindings (See Figure S11). Sections were then incubated with corresponding secondary antibodies (Jackson ImmunoResearch) diluted in blocking buffer for 2 hr at room temperature to visualize primary antibodies, and incubated with DAPI to stain cell nuclei.

Sections were mounted using fluorescent mounting medium and images were collected by BX51 microscope (Olympus), Leica TCS SP5 two-photon confocal microscope or Leica TCS SP8 confocal microscope. Typically, four to six fields per section were randomly pictured for quantification. All areas of fraction and cell density quantifications were analyzed by ImageJ software. The BAD and COX-IV co-localization was analyzed by ImageJ software with Plot Profile option.

Immunohistochemistry (human)

Human brain frozen tissues were embedded into OCT compound, carried out on 15 μm thick sections and mounted on microscope slides before staining. Sections were fixed in ice-cold acetone for 5 min and washed with PBS three times. Immunofluorescent staining of human brain sections was performed as described above.

Immunoblotting analysis

Snap-frozen brain hemispheres or human brain frozen samples were homogenized in RIPA buffer (50 mM Tris-HCl, pH 7.6, 150 mM NaCl, 1% Sodium deoxycholate, 0.1% SDS, 1% NP-40, 1 mM EDTA and 1 mM EGTA) supplemented with 1 mM DTT and various proteinase and phosphatase inhibitors (1 mM PMSF, 1 mM NaF, 1 mM Na_3VO_4, 1 μg/mL Leupeptin, 1 μg/mL Aprotinin and 1 μg/mL Pepstatin) by Precellys 24 (Bertin Technologies) with the program of 5,000 rpm - 3 x 15 s - 30 s and then rotated at 4°C for 30 min. Brain lysates were centrifuged at 4°C, 12,000 rpm for 30 min to remove cell debris and protein concentration of the resulting supernatant was measured by BCA assay. Brain samples were separated by SDS-PAGE gels and proteins were transferred to PVDF or nitrocellulose membranes at 100 Volts for 2 hr. Membranes were blocked in 5% skim milk or 3% BSA diluted in TBST for 1 hr at room temperature, incubated with primary antibodies overnight at 4°C and secondary antibodies for 1 hr at room temperature. Membranes were exposed by enhanced chemiluminescence method and signal intensities were quantified by ImageJ software.

Aβ in brain samples was extracted with SDS buffer containing 2% SDS in 25 mM Tris-HCl, pH 7.5, and detected by Tricine-SDS-PAGE (Schägger, 2006). Briefly, 10% Tricine gel containing 6 M urea was used for protein separation. Proteins were transferred to 0.2 μm PVDF membrane at 30 Volts for 2 hr and the membrane was pre-boiled in PBS for 5 min to enhance sensitivity before blocking.

MLKL dimers were detected by non-reducing SDS-PAGE (Cai et al., 2014). Briefly, 9-month-old mouse brain samples were homogenized and lysed in M2 buffer (20 mM Tris-HCl, pH 7.6, 0.5% NP40, 250 mM NaCl, 3 mM EDTA and 1.5 mM EGTA) supplemented with various proteinase and phosphatase inhibitors without DTT and then separated by SDS-PAGE without β-mercaptoethanol.

ELISA

$Aβ_{40}$ Human ELISA Kit (KHB3482, Invitrogen) and Ultrasensitive $Aβ_{42}$ Human ELISA Kit (KHB3544, Invitrogen) were used to detect soluble or insoluble $Aβ_{40}$ and $Aβ_{42}$. Snap-frozen brain hemispheres were extracted by RIPA buffer for soluble $Aβ_{40}$ and $Aβ_{42}$. The pellets were further extracted by SDS buffer for insoluble $Aβ_{40}$ and $Aβ_{42}$. Protein concentration of RIPA buffer extracts and SDS buffer extracts were measured by BCA methods. ELISA procedures were performed following the manufacturer's protocols.

To detect proinflammatory cytokines, snap-frozen brain hemispheres were homogenized in PBS using Precellys 24 with the program of 5,000 rpm - 3 x 15 s - 30 s. Brain homogenates were centrifuged at 4°C, 12,000 rpm for 30 min to remove cell debris. Protein concentration of the resulting supernatant was measured with BCA assay. Mouse TNFα Quantikine ELISA kit (MTA00B, R&D system), IL-1β Quantikine ELISA Kit (MLB00C, R&D System), and IL-6 Quantikine ELISA kit (M6000B, R&D system) were used for determination of TNFα, IL-1β, and IL-6, respectively.

Microglial morphology analysis

To analyze microglial morphology change, the brain slices of 6-month-old WT, 5XFAD and 5XFAD/$Bad^{-/-}$ mice or 9-month-old WT, APP/PS1 and APP/PS1/$Bad^{-/-}$ mice were analyzed by immunofluorescent staining with anti-Iba1 and anti-Aβ (6E10) antibodies. Plaque-associated microglia in the cortex were imaged using confocal microscope by z-stack with 0.5 μm for each step. Microglial morphology was further analyzed by the Imaris software with the Filament and Surface options.

Real-time quantitative PCR

About 50 mg region-matched brain tissue from 6-month-old WT, 5XFAD and 5XFAD/*Bad*$^{-/-}$ mice were homogenized in 1 ml TRIZOL reagent (15596-018, Invitrogen) and incubated for 5 min at room temperature. Tissue extracts were centrifuged at 4°C, 12,000 *x g* for 5 min. 500 μl supernatant was used for RNA extraction by TRIZOL reagent, according to the manufacturer's instruction. RNA concentration was measured by NanoDrop-2000. Reverse transcription of total RNA to complementary DNA was performed using M-MLV Reverse Transcriptase (M1705, Promega). Quantitative PCR was performed using the ABI QuantStudio 6 System. PCR products were detected by SYBR Premix Ex Taq (RR420A, TaKaRa). The following primers were used for mRNA expression detection: TNFα (forward: CCAAGGCGCCACATCTCCCT; reverse: GCTTTCTGTGCTCATGGTGT), IL-1β (forward: GAAGAAGAGCCCATCCTCTG, reverse: TCATCTCGGA GCCTGTAGTG), IL-6 (forward: TAGTCCTTCCTACCCCAATTTCC, reverse: TTGGTCCTTAGCCACT CCTTC). Relative mRNA expression levels were calculated using the $2^{-\Delta\Delta Ct}$ method.

In vivo phagocytosis assay

Six-month-old WT, 5XFAD and 5XFAD/*Bad*$^{-/-}$ mice were injected with Methoxy-X04 (4920, Tocris) intraperitoneally, which was prepared in 50% DMSO/50% 0.9% NaCl at pH 12.0. Three hours later, mice were anesthetized and perfused with ice-cold PBS. The mouse brains were extracted, chopped into pieces, and then incubated in DMEM/F12 medium (21041025, Gibco) containing 10% FBS, 20 U/ml DNase I (11284932001, Roche), 1.1 U/ml Dispase II (04942078001, Roche) and 0.5 mg/ml collagenase type IV (17104019, Gibco) at 37°C for 1 hr and homogenized with 19-G needles. The resulting homogenates were filtered through 70 μm cell strainers and then centrifuged at 250 *x g* for 10 min. Cell pellets from each brain were resuspended in 4 ml 37% percoll (17089102, GE Healthcare). 4 ml 70% percoll was transferred to a 15 ml tube and carefully overlaid 4 ml 37% percoll containing cells, then overlaid 4 ml 30% percoll and overlaid 2 ml PBS at last. The gradients were centrifuged at 18°C, 300 *x g* for 40 min without break. For each brain sample, 2 ml 70%/37% interphase was collected and diluted with 6 ml ice-cold PBS and further centrifuged at 4°C, 500 *x g* for 5 min. The pellets containing microglia were resuspended in 200 μl PBS.

For flow cytometric analysis of Methoxy-X04 containing microglia, binding of antibodies to Fc receptors was pre-prevented by adding 1 μg anti-mouse Fc block (553141, BD Bioscience) and incubated on ice for 10 min. Cells were centrifuged at 4°C, 250 *x g* for 5 min and resuspended in 200 μl PBS. Cells were immuno-stained with 2 μl CD11b-APC (101211, Biolegend) and 2 μl CD45-FITC (103107, Biolegend) on ice for 30 min. Cells were then centrifuged at 4°C, 250 *x g* for 5 min and resuspended in 400 μl PBS for flow cytometric analysis. Cells were analyzed on BD Celesta or LSRFortessa machine, $CD11b^+$ and $CD45^{low}$ cell population was gated. Unstained WT cells were used to determine background fluorescence, while cells isolated from WT mice injected with Methoxy-X04 were served as the threshold for non-phagocytic microglia.

Stereotactic injection of AAV

Four-month-old 5XFAD mice were deeply anesthetized, then 1μl of 1:1 AAV mixture of AAV9-U6-sg*Bad*-CMV-SaCas9-DIO (6.2×10^{12} Vg/ml) or AAV9-U6-sg*LacZ*-CMV-SaCas9-DIO (6.8×10^{12} Vg/ml) with AAV9-hSyn-RFP-P2A-Cre-WPRE (7.5×10^{12} Vg/ml) was injected into dorsal hippocampus (anterior/posterior: -2.00; mediolateral: 1.50; dorsal/ventral: -1.80) and ventral hippocampus (anterior/posterior: -2.80; mediolateral: 3.00; dorsal/ventral: -4.00). Two months later, the spatial memory of the mice was analyzed by Y-maze test. The BAD protein level in hippocampus was analyzed by immunoblotting analysis, and the Aβ plaques and microglial activation was analyzed by immunofluorescent staining.

QUANTIFICATION AND STATISTICAL ANALYSIS

Statistical analysis

Comparison between two groups was analyzed by unpaired two-tailed Student's *t*-test and comparison among three groups was analyzed by one-way ANOVA test. GraphPad Prism 6 software was used for analyzing data. Difference was considered to be significant when p value <0.05 (*), p value <0.01 (**) and p value <0.001 (***).